

AD 654524

# MECHANISMS OF LASER-SURFACE INTERACTIONS

By

J. F. Ready

E. Bernal G.

L. T. Shepherd

FINAL REPORT

To

Ballistic Research Laboratories

Contract No. DA-18-001-AMC-1040(X)

May, 1967

Presented by

Honeywell Inc.

CORPORATE RESEARCH CENTER

Hopkins, Minnesota

This document has been approved  
for public release and sale; its  
distribution is unlimited.

ARCHIVE COPY

DDC  
RECEIVED  
JUL 14 1967  
C

**MECHANISMS OF LASER-SURFACE INTERACTIONS**

**By**

**J. F. Ready**

**E. Bernal G.**

**L. T. Shepherd**

**FINAL REPORT**

**To**

**Ballistic Research Laboratories**

**Contract No. DA-18-001-AMC-1040(X)**

**May, 1967**

"Delivered by Honeywell Inc., Corporate Research Center, pursuant to Contract No. DA-18-001-AMC-1040(X). Government's use controlled by the provisions of Articles 51 and 26 of Title II of the contract which are ASPR 9-107.2 and 9-203.1 and 9-203.4, respectively."

**Presented by**

**Honeywell Inc.**

**CORPORATE RESEARCH CENTER**

**Hopkins, Minnesota**

## ABSTRACT

This report describes experimental and theoretical investigations of the particle emission produced in the laser-surface interaction. Preliminary measurements on the angular distribution of ions emitted from a tungsten target at power levels around  $14 \text{ MW/cm}^2$  indicate anisotropy of the emission, with a strong enhancement in directions near the normal to the target. Ion and neutral molecule emission from laser-irradiated sodium targets are described. Calculations on the free expansion of the laser-produced blowoff material, which include the asymptotic velocity of the expansion, yield pulse shapes similar to those observed experimentally if a high initial temperature is assumed. The magnitudes and time histories of shock waves produced in the target by absorption of the laser radiation have been calculated.

## TABLE OF CONTENTS

Section	<u>Page</u>
I      Introduction	1
II     Experimental Investigations	6
A.    Equipment Construction	6
B.    Measurements of Angular Distribution of Charged Particles	13
C.    Properties of Nickel Targets	19
D.    Emission from Sodium	20
III    Theoretical Investigations	30
A.    Analysis of Space Charge Sheath and Use of Saha Equations for Determining Extent of Ionization in a Plasma	30
B.    Calculation of Laser-Induced Pressure Pulses in the Target	44
C.    Expansion of Blowoff Material	61
D.    Electron Emission	72
E.    Particle Emission in Laser-Surface Interactions	79
IV     Summary	82
References	85

## LIST OF ILLUSTRATIONS

<u>Figure</u>	<u>Page</u>
II-1     Detectors for Angular Distribution Measurements	7
II-2     Photograph of New Ruby Laser	8
II-3     Pulse Shape from New Ruby Laser	11
II-4     Geometrical and Electrical Arrangement for Angular Distribution Measurements	14
II-5     Signals from Hemisphere and Charge Collector in Forward Direction	16
II-6     Signals from Charge Collectors on Different Parts of Hemisphere	18
II-7     Ion Emission from Sodium	21
II-8     Neutral Molecule Pulses from Sodium	27
II-9     Arrival Times of Neutral Molecule Pulses from Sodium	29
III-1     Potential Diagram for Parallel Plate System	31
III-2     Energy Diagram near Tungsten Surface	34
III-3     Schematic Potential Diagram for Ions	36
III-4     Equilibrium Electron Density for Carbon Plasma	40
III-5     Flow of PUFF Code	47
III-6     Pressure Profiles in Tungsten at Various Times	51-53

<u>Figure</u>		<u>Page</u>
III-7	Pressure at Rear Surface of Tungsten Target	59
III-8	Calculated Mass 28 Flux, Uniform Density Model	65
III-9	Calculated Mass 28 Flux, Asymptotic Solution	67
III-10	Calculated Mass 23 Flux, Asymptotic Solution	68
III-11	Calculated Electron Emission from Tungsten	76
III-12	Temperature of Thoriated Tungsten Surface	77

## SECTION I

### INTRODUCTION

The investigations described in this report are continuations of work which has been carried out previously. These earlier investigations have been concerned with particle emission produced in laser-surface interactions. This work has been described in detail in previous reports.<sup>(1, 2, 3, 4)</sup> Some knowledge of the background of this work, as discussed in the previous reports, is necessary for an understanding of the methods and aims of the investigations described in the present report. A time-of-flight spectrometer has been used to measure ion emission produced by absorption of ruby laser radiation with power densities of the order of  $50 \text{ MW/cm}^2$ . The ions were found to be mainly alkali metals with energies of the order of several hundred electron volts. The neutral molecule emission produced under similar conditions has been studied with a quadrupole mass spectrometer and found to consist of thermally desorbed gases such as  $\text{H}_2$ ,  $\text{CO}$ , and  $\text{CO}_2$  along with pulses of high energy neutral molecules having energies of the order of 100 eV.

In this report we describe the extensions of these types of measurements. In some instances the same types of measurements as described in the previous reports have been carried out on a different target surface, namely sodium. In other cases, the types of measurements are new. We describe construction of equipment for measurements of the angular distribution of ions emitted in the laser-surface interaction, and describe preliminary measurements on the angular distribution. The equipment construction and the new measurements represent a transition point in this work. Previously the quadrupole spectrometer and the time-of-flight spectrometer were the basic instruments used to investigate many different types of surfaces, and the investigations were carried out at relatively low laser powers per unit area. With the introduction of this new equipment, we shall extend the range of measurements to higher laser powers and also begin to carry out additional types of measurements designed to elucidate the phenomena occurring in the laser-surface interaction.

Specifically, the experimental measurements carried out during this report period have involved measurements of the angular distribution of ions emitted from tungsten targets. It was found, contrary to our previous expectations, that the angular distribution from a tungsten target is anisotropic. The angular distribution is strongly peaked in the forward direction normal to the target surface. It should be emphasized that these results are still preliminary, but it appears as if the strongest emission is within angles approximately  $15^\circ$  from the normal to the surface. The flux along directions more nearly parallel to the target surface drops off to a relatively low level. If, in subsequent measurements, these preliminary results are confirmed, it will have implications for the previously calculated values of numbers of ions emitted in the laser surface interaction. Those numbers were obtained assuming that the angular distribution was approximately isotropic. We shall have to reconsider these conclusions in the light of the present knowledge of the angular distribution.

Measurements have also been made on a sodium target. Sodium is of interest because the largest component of the ionic emission from other surfaces was found to be sodium under our conditions of laser power. These measurements were similar to those described previously in that they used the time-of-flight mass spectrometer and quadrupole spectrometers. Results indicate large amounts of sodium ion emission along with fragments due to heavy hydrocarbons which come from the kerosene in which sodium had been stored. The neutral gas pulses also showed much more hydrocarbon contribution than was the case with other target materials. The high energy neutral molecules were also observed with qualitative results similar to those from other target materials such as carbon.



On the theoretical side some new topics have been considered. These include consideration of the amount of space charge which is produced in the laser-surface interaction, and a reexamination of the expected ionization level of the blowoff material. These considerations, which go into much greater detail than previously, indicate that it may be worthwhile to reconsider the topic of absorption of laser light in the blowoff material by the process of inverse Bremsstrahlung, and the possibility of rapid heating of the blowoff material to high temperatures. The previous results, (2) which had indicated that this heating would be low under our experimental conditions, will have to be reevaluated in the light of the present considerations on the space charge effects and the amount of ionization.

Another new topic which is considered in this report is the calculation of the stress profiles produced by thermomechanical shock waves in the target material. The material expands as energy is deposited in a thin surface layer in a short time, and a pressure pulse can be produced which propagates into the material at the speed of sound. We have calculated the time history of the stress profile using the PUFF computer code. Results indicate that in our experimental situation we should obtain a sharp single pressure pulse propagating into the material with an amplitude of the order of  $6 \times 10^8$  dynes/cm<sup>2</sup>. The stress profile will not be strongly dependent on the shape of the laser pulse. Detailed pressure profiles within the target material are presented for various times after the beginning of the laser pulse.

We also extend calculations of the adiabatic free expansion of the laser-produced blowoff material, which were described previously. In this report we introduce the asymptotic value of the velocity of expansion of a cloud of material. We find that we get good agreement between the shapes of the pulses calculated in this manner, and the shapes of experimentally determined pulses. A necessary condition to obtain sharply rising narrow pulses of the type that we observed experimentally is that the original temperature of the

material before it begins to expand is high, of the order of  $10^5$ °K. This temperature, which produces a directed energy of expansion of the gas cloud, is considerably lower than the temperature that would have to be invoked to explain the experimentally observed ion velocities as purely thermal velocities. The results of this treatment indicates that a heating mechanism for the gas should be investigated further. The picture that is derived from this result is very suggestive of a heating of the ions decoupled from the neutral gas, followed by a free expansion which gives the observed directed component of the velocities of expansion.

Finally, we discuss a speculative model in which the features suggested by the calculations on the adiabatic free expansion, and the measurements on the time-of-flight spectrometer and the quadrupole spectrometer, can be synthesized to make a complete picture of the interactions in the laser-produced blowoff material. This picture has the advantage of providing consistent interpretations for the results from the two types of spectrometers. It seems to predict the main features of the observations, and suggests the heating mechanism for the observed energetic ions but allows most of the material (e. g., desorbed neutral surface gases) to remain cool. This picture must be regarded as preliminary, but it does combine enough features to be physically appealing. The main question is whether we can invoke a heating mechanism that will provide the heating of the ions to the required initial high temperatures .

This report occurs at a transition phase between the measurements conducted on many different types of materials at relatively low laser powers per unit area, and new types of measurements in which the laser powers per unit area will be raised to higher values. The results obtained previously on particle emission and on the phenomena occurring in the blowoff material can be used to provide an integrated model of all the processes that take place. The previous considerations have accounted for various phenomena essentially one at a time. For example, calculations on the expansion of the blowoff material

were carried out separately from a consideration of the heating occurring in the blowoff material. The present report marks the point at which these various types of measurements and calculations begin to be synthesized into one complete picture of the process occurring in the laser-surface interaction.

## SECTION II

### EXPERIMENTAL INVESTIGATIONS

#### A. EQUIPMENT CONSTRUCTION

Construction of the interaction chamber for measurements of angular distribution of charged particles<sup>(4)</sup> has been completed. An Ultek 20 liter/sec ion pump maintains the system at a pressure of  $< 10^{-8}$  Torr. The detectors used so far have been unipolar detectors of the type shown in Figure II-1. The detectors consist of a stainless steel cylinder closed at one end with a solid plate containing holes for electrical connections, and a 95% transparent tungsten mesh at the other end. Inside the cylinder are two grids of the same tungsten weave, as well as a solid stainless steel disk that serves as the collector. One of the grids is connected directly to the collector while the second one is insulated from it so that it can be used for decelerating potential measurements. Each collector is tied to an independent BNC output connector. The decelerating grids are all connected together and share a common BNC connector.

Previously, we had also described construction of a new larger ruby laser to be used in the laser-surface interaction studies.<sup>(4)</sup> Construction of this item took considerably longer than was anticipated because of a number of unforeseen difficulties. These included an unexpectedly long wait for the roof prism with Brewster angle entrance face. However, it is in operation now at a power level of approximately 100 megawatts.

A partially assembled view of the system is shown in Figure II-2. This is a photograph of the entire system with the dielectric coated elliptical glass reflector removed. The flash tube may be seen above the ruby in its water cooling jacket. On each side of the cavity is a holder for the cryptocyanine Q-switch. On the left the Brewster angle roof prism is visible, and at the far right the holder for the output reflector, which is a sapphire etalon.

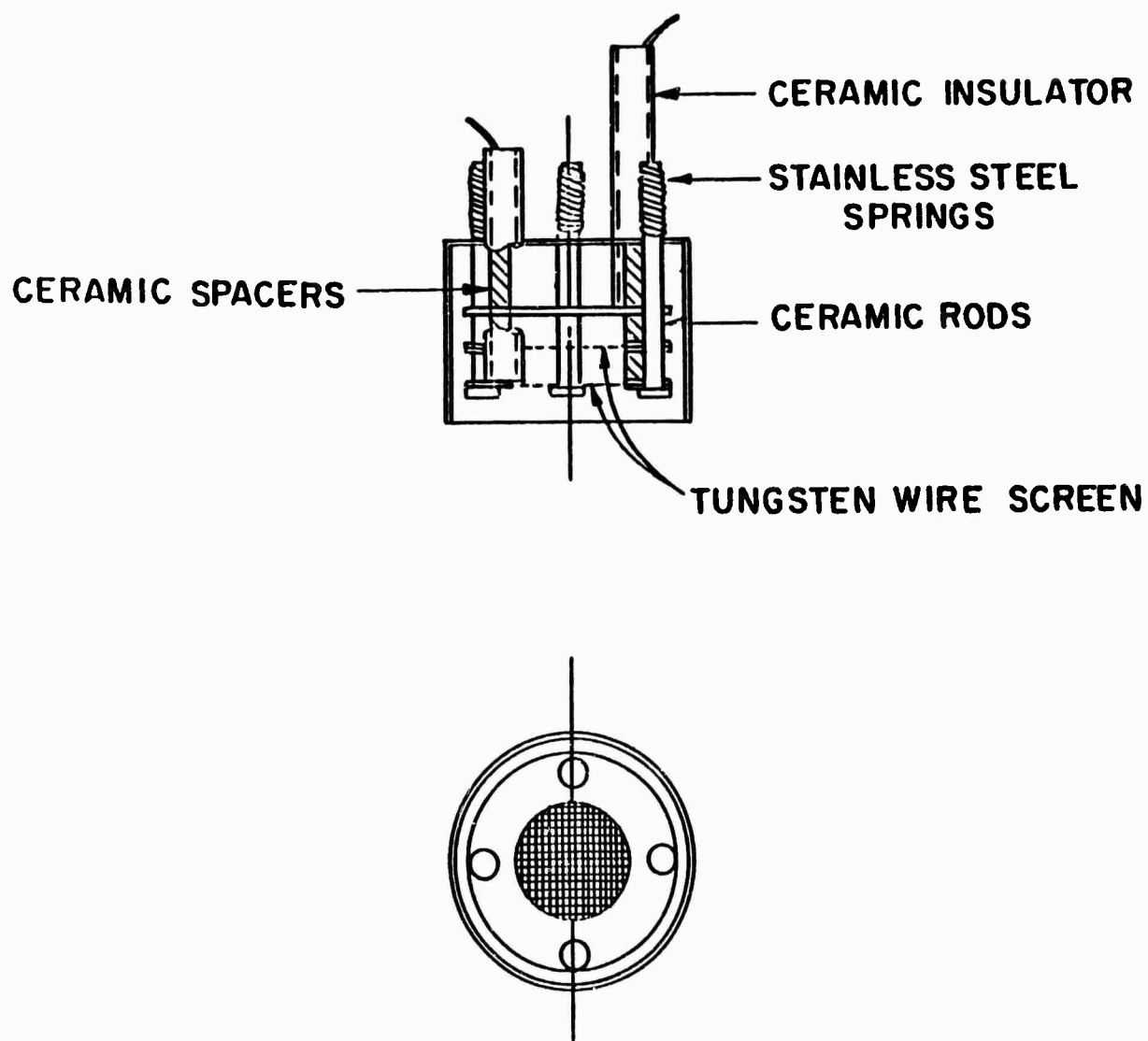


Figure II-1 Schematic of unipolar detectors used for angular distribution measurements

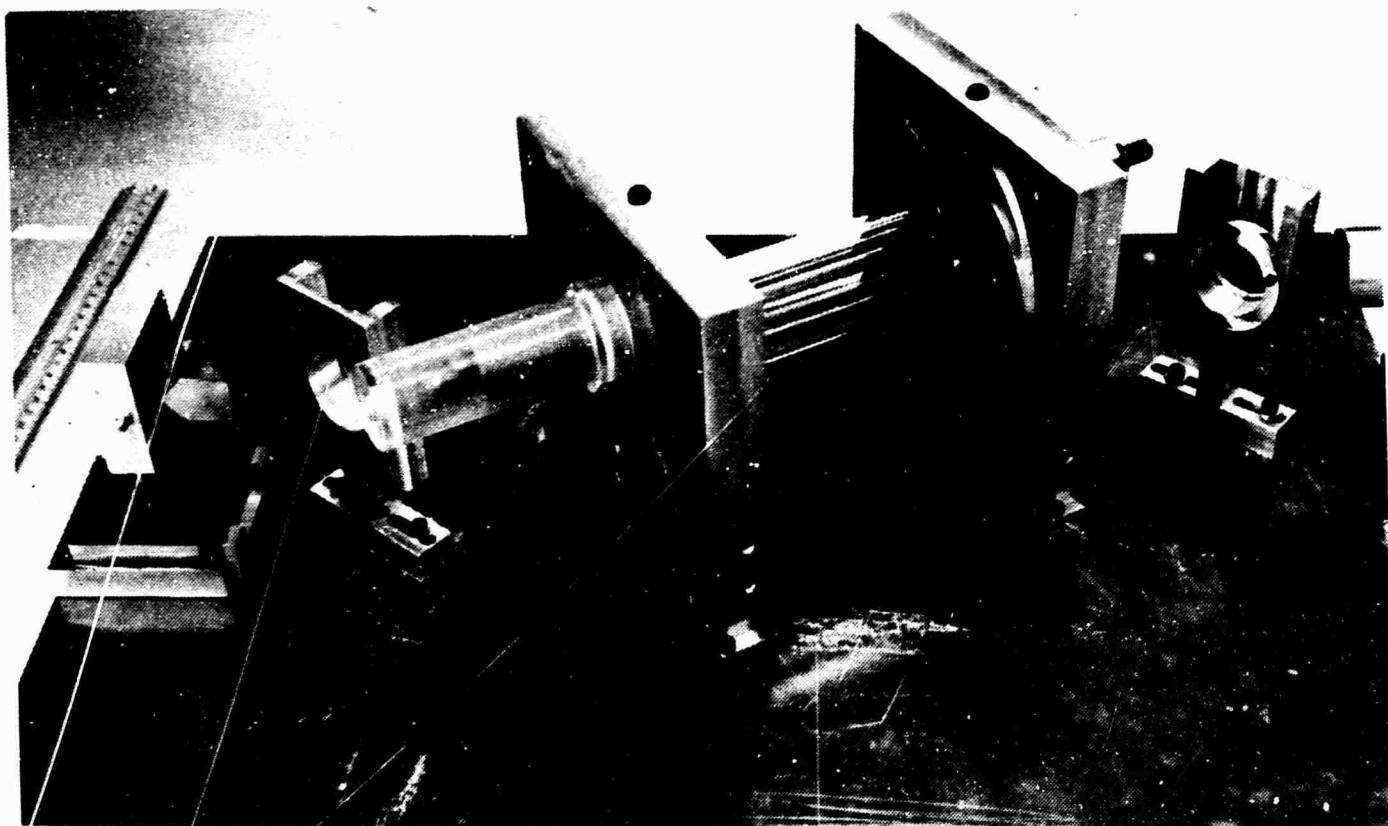


Figure II-2 - Partially disassembled view of large ruby laser

This system is pumped by a bank of capacitors with a total capacitance of 1200 microfarads, and a maximum voltage of approximately 2700 volts. The total energy available as input is thus approximately 4400 joules.

The maximum input energy was chosen to be approximately 50% of the explosion energy of the FX-67 flash tube.<sup>(5)</sup> By using 50% of the explosion energy of the flash tube as the maximum input energy, we expect to obtain reasonable lifetime from the flash tube.

The alignment of this entire system is accomplished using a helium-neon laser. The angular orientation of the etalon is adjusted so that the beam reflected from its front surface is reflected directly back into the helium-neon laser. Then the position of the ruby is adjusted so that the beam passes directly down the center of the ruby. This may be observed from the scattering of the helium-neon laser beam within the ruby. The ruby is rotated so that the reflection on the Brewster angle end is a minimum. Then the cytiocyanine cells are inserted in the beam and they are rotated to give a minimum reflection at Brewster's angle. Finally, the roof prism at the end of the system is adjusted so that the reflection from it travels back into the ruby. This may be checked by inserting a pin hole in the original helium-neon laser beam. If the reflection from the roof prism is not exactly aligned, the return beam can be seen striking the material next to the pin hole. The system is aligned until the helium-neon laser beam traverses a re-entrant path.

When this laser was fired in the non-Q-switched mode, that is with pure methyl alcohol in the liquid cells in the cavity, a threshold value of about 2000 volts on the power supply was obtained, corresponding to a threshold input energy of approximately 2,400 joules. Thus there is considerable capability for increasing the input energy to overcome the losses in the cavity that result from the bleachable dye. The shape of the pumping light pulse is roughly triangular with a full width at half height of approximately 600  $\mu$ s. The current through the flash tube showed some evidence of ringing. The FX-67 flash tube

is polarized, that is, current should flow through it in only one direction. If current flows the opposite direction, damage to the flash tube and shortening of its life will result. We measured the current through the flash tube using a coil around the wire leading to the cathode. We found that in the original stages of the pumping pulse the current flowed in the correct direction, but it went through zero and there was a reverse current approximately  $1/3$  as high as the forward current. By adding inductance to the system the reverse current was damped out considerably. This has reduced, but not entirely eliminated, the reverse current.

When cryptocyanine is added to the liquid cells, Q-switched laser action is obtained at an input voltage of approximately 2400 volts with a single pulse. This corresponds to an input energy of approximately 3,400 joules. The pulse height can be varied by increasing the cryptocyanine concentration and working at higher input voltages. This will be the means of controlling the amplitude of the output pulse. The pulse shape is shown in Figure II-3, which is drawn from a photograph of an oscilloscope trace of the output of an ITT FW114 phototube viewing a reflection of the output pulse. The response time of the entire system (phototube plus cable plus scope) is estimated to be less than 10 nanoseconds so that this should represent a true picture of the shape of the output pulse. The base-to-base width of this pulse is approximately 60 nanoseconds, and the width at half height is approximately 26 nanoseconds. The ringing observable at the end of the pulse is probably due to lack of complete impedance matching in the termination of the cable.

The amplitude of these pulses has not as yet been accurately measured. The reason for this is that at the higher laser power our old calibration techniques are not applicable. Previously we would fire the laser directly into a TRG model 100 ballistic thermopile in order to obtain the total energy in the pulse. Then from the knowledge of the pulse shape we would obtain the peak power in the pulse. From these measurements the ITT phototube viewing a reflection of



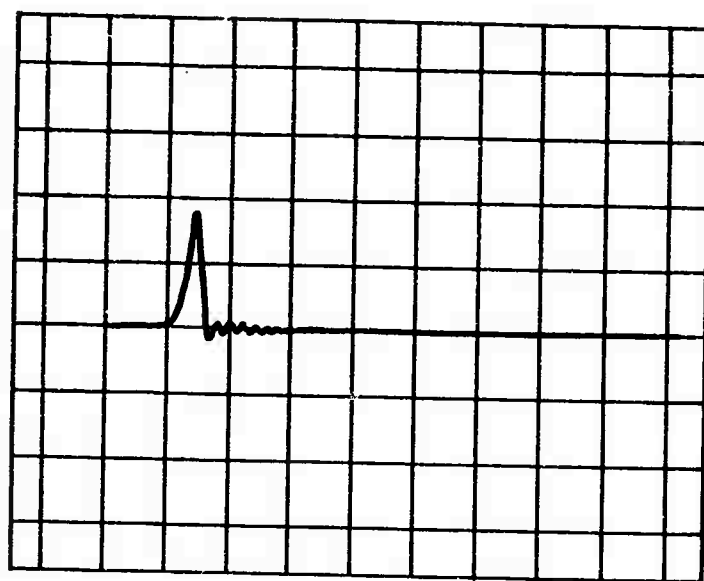


Figure II-3 - Pulse shape emitted from large ruby laser. Time goes left to right at 100 ns/div. Drawn from photograph of scope trace for clarity in reproduction.

part of the laser beam could be calibrated to give the output of the beam when it was actually being used for the laser-surface interaction studies. However, we fired the large laser at a piece of copper similar to that used in the input hole of the TRG thermopile, and found that the copper surface was damaged. Thus, we could not use the same calibration technique as used previously because this would damage the thermopile. Therefore, new calibration techniques must be devised to monitor the output of this laser. Instead of shooting the beam directly into the thermopile, we shall use the thermopile to view the diffuse reflection from a magnesium oxide block. In order to carry out this calibration, we must then know accurately the fraction of light reflected from the magnesium oxide block into the thermopile. This calibration is not yet complete so we cannot state exactly the power levels at which the new laser has been operating. However, a preliminary estimate indicates that we have exceeded power levels of 100 megawatts with the system. By increasing the cryptocyanine concentration and the input voltage, we feel that single pulses with even higher power can be obtained.

When the output of the laser is focused with a simple, inexpensive lens with a focal length of 5 cm, we can produce a very large spark in air at atmospheric pressure. The approximate focal area is  $10^{-3} \text{ cm}^2$ . Since other measurements indicate that to breakdown air a total power per unit area of the order of  $10^{11} \text{ watts/cm}^2$  must be achieved, this measurement also indirectly indicates that the peak power available is of the order of  $10^8 \text{ watts}$ .

In summary then, the larger new ruby laser construction has been completed, and the design goal of approximately 100 MW appears to have been met although the measurements of the power output are as yet incomplete. In the next report period we intend to bring the laser into use in extending the range of our studies of laser-surface interactions to higher power levels.

## B. MEASUREMENTS OF ANGULAR DISTRIBUTION OF CHARGED PARTICLES

A certain amount of preliminary data has been obtained on the behavior of the interaction chamber as well as on the angular distribution of charged particles. Figure II-4 shows a cross-section of the geometrical and electrical arrangements used to obtain data. The output of a Q-switched ruby laser is aimed at the target through a 5/16" diameter hole cut in the hemisphere at 30° from the polar axis and in a plane perpendicular to the plane of the detectors. The laser beam is slightly focused with a simple lens to reduce its diameter and prevent it from striking the hemisphere. The target is a 32 mm diameter tungsten disc held 1.6 cm above a grounded stainless steel disc by a ceramic insulator. The center of the tungsten disc is at the center of curvature of the 17.5 cm diameter hemisphere. The collectors are placed at 15° intervals along a meridian. They collect charges arriving within a 5/16" diameter aperture in the hemisphere. The solid angle they subtend at the target is  $2\pi \times 10^{-3}$  steradians, which is one thousandth of the solid angle subtended by the hemisphere.

The data obtained so far has resulted from irradiation with a 1 megawatt peak power laser pulse focused to a spot of 3mm diameter ( $14 \text{ Mw/cm}^2$ ). Two types of measurements have been made: In the first, we compare the charge collected by one of the detectors with that collected by the hemisphere to see if the ratios of the signals are equal to the ratios of the solid angles of the two collectors. In the second set of experiments, we compare the signal from detector #6 (forward detector in Figure II-4) to that of collectors #5 through #1. We emphasize that the results presented below are of a preliminary nature with several features that are not well understood; however, some interesting

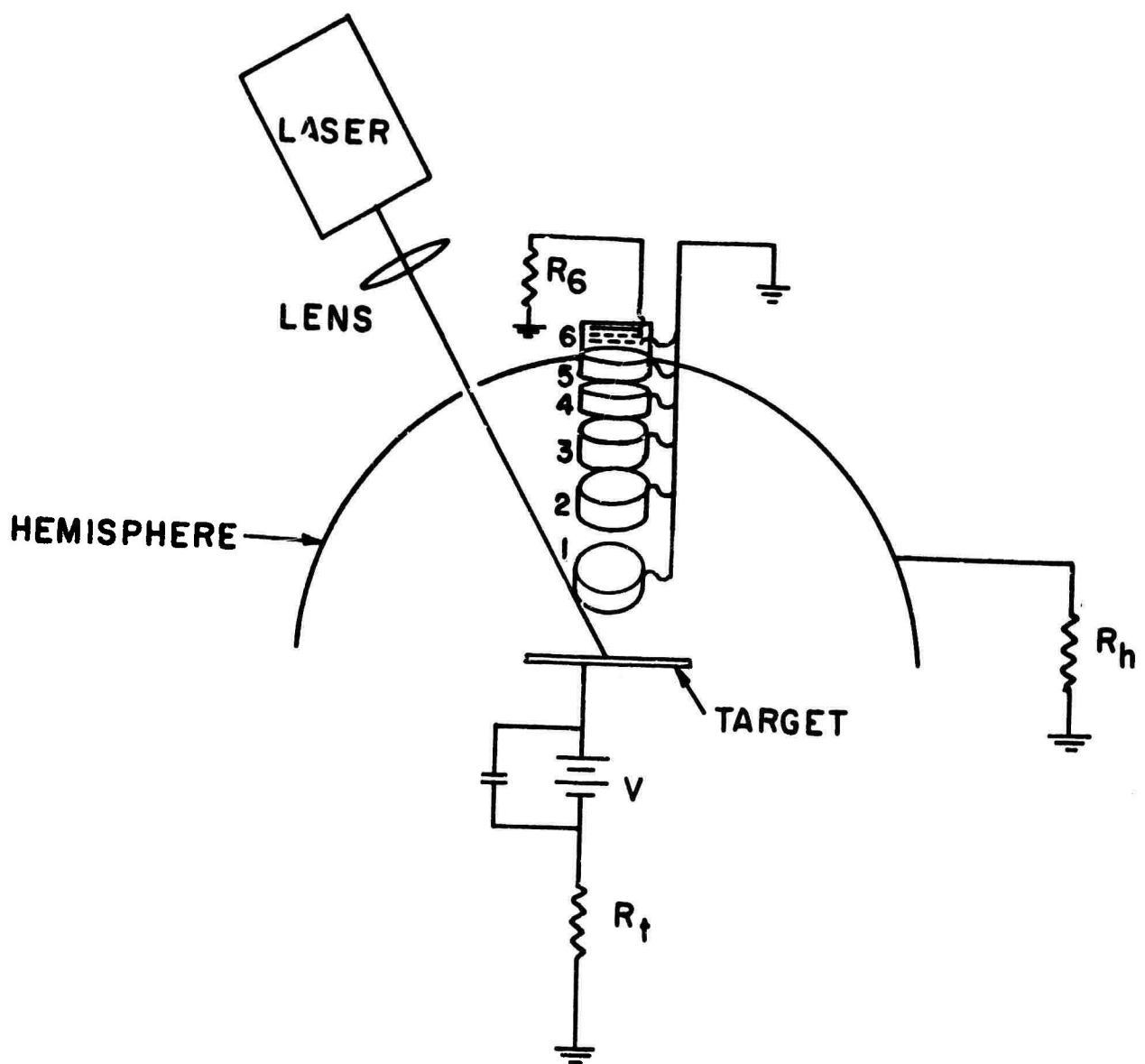


Figure II-4 - Cross-section of geometrical and electrical arrangement used for angular distribution measurements

qualitative conclusions can be drawn from them.

Figure II-5 shows the signals obtained from resistors  $R_h$  and  $R_6$  in Figure II-4 upon irradiation of the tungsten target. In this experiment the target was grounded ( $V=0$ ) and so were the decelerating grids;  $R_h$  and  $R_6$  were identical 50 ohm resistors, and  $R_T$  was removed (target grounded). Both traces were triggered by the signal from a 919 phototube monitoring the laser pulse and run at  $5\mu\text{s}/\text{cm}$ . The upper trace is the signal from the hemisphere ( $R_h$ ) with a vertical sensitivity of 0.2 V/cm; the lower trace is the signal from detector #6 ( $R_6$ ) at a vertical sensitivity of 0.02 V/cm. The signal from the hemisphere (upper trace) can be interpreted as follows: During the first microsecond after the laser pulse, the net current is negative due to the higher electron velocities, but after the electrons are either collected at the electrodes or recombine, the current becomes positive because of the slower positive ions. Since no accelerating potentials are applied, there is a large spread in ion arrival times, hence the long tail of the positive part of the pulse. The signal from detector #6 (lower trace) contains a considerable amount of ringing that we have not been able to eliminate yet; for that reason the first microsecond of the trace does not contain useful information. Also, the negative-going signal observed after  $\sim 8\mu\text{s}$  is believed to be ringing. The positive part of the signal that starts at  $\sim 3.5\mu\text{s}$  after the beginning of the laser pulse is due to ions arriving at the collector of detector #6; this can be verified by noting that the beginning of the positive-going signal from detector #6 (lower trace) coincides in time with the peak of the signal from the hemisphere (upper trace) as predicted by a previous analysis,<sup>(2)</sup> if the signals were produced by the same pulse of charge traveling from the target to the collector, past the hemisphere. A further check on the interpretation of the data of Figure II-5 is the time of flight. We know from previous measurements on tungsten in the TOF spectrometer that most of the emission consists of desorbed  $\text{Na}^+$  and  $\text{K}^+$  ions<sup>(1)</sup> and if we assume that the large positive pulse from detector #6 is due to  $\text{Na}^+$ , we arrive at an ion energy of  $\sim 100$  eV, which is in good agreement with the energies measured in the TOF spectrometer.



Figure II-5 - Signals from hemisphere (top trace) and detector #6 (bottom trace). Time base is  $5\mu\text{s}/\text{cm}$  for both traces; vertical sensitivity 0.2 V/cm for top trace and 0.02 V/cm for bottom trace.

Integration of the area under the pulses of Figure II-5 yields a total charge collection of  $2.4 \times 10^{11}$  elementary charges at the hemisphere and  $8.8 \times 10^9$  from detector #6. Assuming that these preliminary figures are correct, we arrive at two interesting conclusions: (a) The ratio of the signal from the hemisphere to that of detector #6 is 27, while the ratio of the solid angles subtended by those two detectors is  $\sim 1000$ . This means that the emission is highly anisotropic with a strong peak in the forward direction; (b) The number of charged particles emitted per laser pulse is about two orders of magnitude greater than what we had estimated from the measurements in the TOF spectrometer. <sup>(1)</sup>

Figures II-6a and II-6b compare the charge collection of detectors #5 and #2 with that of detector #6 (see Figure II-4) for two different laser shots. The vertical sensitivity and time base of all traces is 0.05 V/cm and  $2\mu\text{s}/\text{cm}$ , respectively. A potential of 1030 v. was applied to the target. The lower trace in both figures is the signal from detector #6; the upper trace in Figure II-6a is the signal from detector #5, while in Figure II-6b it is the output of detector #2. The number of elementary charges collected in Figure II-6a is  $2.6 \times 10^{10}$  for the upper trace (#5), and  $2.8 \times 10^{10}$  for the lower trace (#6). The corresponding numbers for Figure II-6b are  $8.8 \times 10^9$  and  $2.9 \times 10^{10}$ , respectively. Since the signal from detector #6 is essentially constant in Figures II-6a and II-6b, a comparison of the signals from detectors #5 and #2, that are located at  $15^\circ$  and  $60^\circ$  to the polar axis respectively, gives a good indication of the anisotropy of charged particle emission. It can be seen from the above numbers that the angular distribution of particles is anisotropic, peaking in the forward direction, but not enough to explain the anisotropy suggested by the data of Figure II-5. However, before pursuing this apparent discrepancy any further, we must obtain further data on the angular distribution without applying a potential to the target, as well as the distribution in the plane perpendicular to the one where the detectors are presently located. Such measurements will be performed in the next contract period.



(a)



(b)

Figure II-6 - Signals from charge collectors mounted on hemisphere. Vertical sensitivity and time base of all traces is 0.05 V/cm and 2  $\mu$ s/cm, respectively. A potential  $V = +1080$  v. applied to target. The lower trace of both (a) and (b) is the signal from detector #6; the upper trace of (a) is signal from detector #5, and in (b) it is the signal from detector #2.



### C. PROPERTIES OF NICKEL TARGETS

Because results of our measurements on neutral gas emission from single crystalline nickel targets differed from those obtained by David Lichtman in electron bombardment measurements,<sup>(4)</sup> we made measurements on the composition of the nickel itself in order to assure ourselves that the targets that we were using were in fact similar to those used by Lichtman in his measurements.

We measured the purity of the samples by means of a residual resistivity measurement and measured the single crystal orientation of the targets by X-ray diffraction. The purity measurement involves measuring the resistivity of the material at room temperature and the resistivity at liquid helium temperature, and taking the ratio of the two results. Theoretically for a perfect infinitely large lattice of nickel atoms, the ratio of these resistivities should be approximately 62,000. Because of the surface scattering, since the nickel targets are not infinitely large, and because of magnetic scattering in magnetic materials, this ratio should be reduced for a perfect nickel lattice of finite extent to approximately 2,000. If the material is not completely pure but is of the order of 99.9% pure, as claimed by the manufacturer, we would expect the ratio to be of the order of 200.

The actual measured ratios both for our specimens and for those by Lichtman were in the range 15 to 20. Interpretation of this result in terms of the purity of nickel is somewhat dubious, but the relatively low value of the ratio indicates that the purity probably does not exceed 99.9%. At any rate, the purity of the specimens that we used was comparable to the purity of Lichtman's material.

The X-ray diffraction measurements indicated that the crystals were in fact good single crystals since very sharp diffraction spots were obtained in general. However, the orientation of the material was not exactly as specified by the manufacturer. Some samples were misaligned by as much as  $8^\circ$ . The (100) axis should have been normal to the surface of the targets; in fact, it was tilted at angles up to  $8^\circ$  from the normal. However, the same phenomena was observed in samples that were used by Lichtman, and it is felt that the departures from perfection of the targets has not caused the differences between our results and Lichtman's.

#### D. EMISSION FROM SODIUM

The ion emission from a metallic sodium target was measured in the time-of-flight spectrometer. The interest in sodium arose because it has been one of the largest components of the ion emission from all our previous targets. We felt, therefore, that by using a sodium target we might enhance the sodium peak to be much larger than all others and effectively provide a source of single-mass ions.

The measurements were made on reagent grade sodium metal that was stored under kerosene for a period of several years. A typical spectrum is shown in Figure II-7. The photograph is a mass spectrum obtained in the time-of-flight spectrometer with an accelerating potential  $V = +2000$  v., and no decelerating potential ( $V' = 0$ ). The vertical sensitivity and time base of the upper trace are 0.1 V/cm and  $5 \mu\text{s/cm}$  respectively; the lower trace displays the same signal as the upper trace, but at a sensitivity of 0.05 V/cm and time base of  $2 \mu\text{s/cm}$ . It can be seen from the figure that of all the mass peaks observed for  $m \leq 40$  a. m. u. in the emission from other targets, <sup>(1,2)</sup> we only have sodium left. However, several peaks corresponding to masses 46, 61, and 101 a. m. u. are found in abundances comparable to the sodium itself. Although we cannot make a positive identification, we feel that those peaks other than  $\text{Na}^+$  are due to heavy hydrocarbon fragments derived from

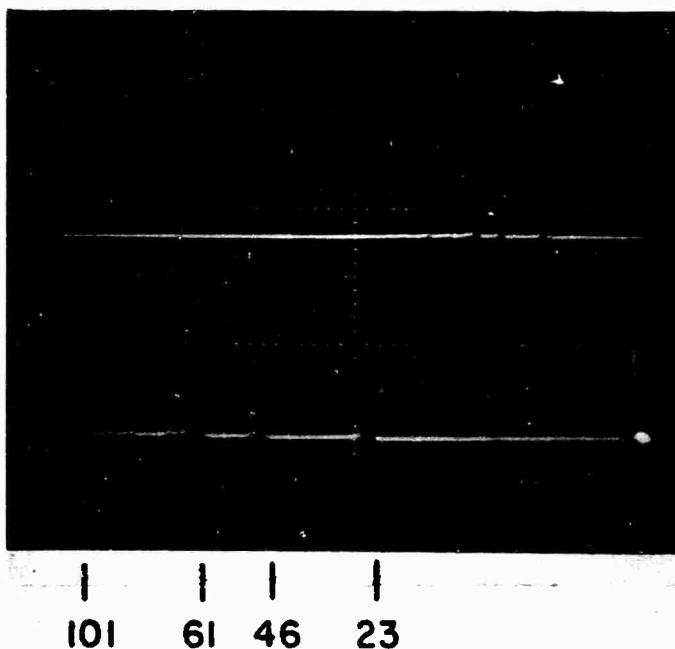


Figure II - 7 - Ion emission from sodium target. Time increases from right to left. Both traces are triggered by laser pulse. Vertical sensitivity and time base of upper trace are 0.1 V/cm and 5  $\mu$ s/cm respectively. Lower trace displays the same signal as upper trace but at 0.05 V/cm and 2  $\mu$ s/cm. The TOF spectrometer potentials are  $V = +2000$  v. and  $V' = 0$  v.

the kerosene in which the metal was immersed. Kerosene is a mixture of hydrocarbons composed primarily of chains containing six to ten carbon atoms, <sup>(6)</sup> hence, it is not surprising to find such heavy fragments. Also, the sodium metal we have used is very likely a sponge-like solid which would readily absorb solvent. The possibility of the high-mass peaks being due to metallic contaminants can be ruled out on the grounds that they do not adsorb readily and their presence in the bulk is specified by the suppliers of the sodium metal to be less than one percent. Hence, hydrocarbons are the only reasonable source for those peaks.

In conclusion, although sodium appears to be a potentially useful material for further investigations of laser-induced ion emission, it is going to be necessary to use material that is not contaminated with organic solvents. The heavy contamination can probably be avoided by the use of single crystal material.

We have also introduced a sodium target into the quadrupole spectrometer. This was done in order to compare results from this same target material on the two different types of spectrometer. We were also interested in determining whether we could detect the base material, sodium, in measurements made on the gas desorption. Since sodium has a relatively high vapor pressure as compared to other materials that have been used in the quadrupole spectrometer, we felt that it was possible that we might observe the sodium in the gas phase. The results of the measurements on sodium in the quadrupole spectrometer are qualitatively very similar to those from the other metals studied previously.

In measurements on the emission from the gas phase we again found large peaks corresponding to hydrogen and to carbon monoxide. In addition, large amounts of hydrocarbons were emitted from a sodium target. This is to be

expected since the sodium target was immersed in kerosene prior to its introduction into the vacuum. Large mass peaks at masses 14, 15, 16, 26, 27, 29, and 30 were observed because of hydrocarbon emission. The amount of hydrocarbons desorbed from the sodium target is much greater than the amounts observed from other target materials. The relative amounts of the various species are given in Table II-1. From other materials such as tungsten, detectable hydrocarbon signals were observed. However, they were always much smaller relative to masses 2 and 28. With the sodium target, the amounts of hydrocarbon are comparable to the amount of mass 28. In fact, the emission of mass 28 undoubtedly contains a component of  $C_2H_4$  as well as CO. Another distinctive feature is that the largest single peak here is molecular hydrogen.

We made a careful search for emission of sodium as neutral gas, but were unable to find any conclusive evidence of a detectable amount of neutral sodium emission. However, even if considerable amounts of sodium gas were produced, it would stick on the first surface that it struck, so that the measured sodium gas pulse from a sodium target would not be large. The only neutral sodium which would reach the detector would be that which follows the direct line-of-sight path from the target through the ionization chamber and the quadrupole region and into the detector.

Because of the presence of considerable amounts of oxidation on the surface of the sodium, we attempted to heat the target. When the target was heated by passing an electrical current through it, the surface appearance of the target changed and there were changes in the dimensions of the target. When the sodium was originally placed in the target holder, it was clean and bright in appearance, having a somewhat silvery color. It was transferred directly from the kerosene in which it was stored into cyclohexane, which was found to evaporate more slowly from the surface of the sodium, giving it protection from oxidation during the time of transfer from the original container of

TABLE II-1  
RELATIVE INCREASE OF VARIOUS MASS SPECIES  
ABOVE BACKGROUND - SODIUM TARGET

<u>Mass Number</u>	<u>Species</u>	<u>Relative Increase (arbitrary units)</u>
2	H <sub>2</sub>	300
14	CH <sub>2</sub>	7
15	CH <sub>3</sub>	18
16	CH <sub>4</sub>	20
17	OH	4
18	H <sub>2</sub> O	20
24	C <sub>2</sub>	1
25	C <sub>2</sub> H	4
26	C <sub>2</sub> H <sub>2</sub>	24
27	C <sub>2</sub> H <sub>3</sub>	7
28	C <sub>2</sub> H <sub>4</sub> + CO	50
29	C <sub>2</sub> H <sub>5</sub>	6
30	C <sub>2</sub> H <sub>6</sub>	1

kerosene into the spectrometer. While the sodium target was being fastened in the spectrometer, the spectrometer was flushed with helium gas. By the time the system was pumped down, the surface of the sodium target had assumed a light gray appearance. This was due to oxidation during the time of transfer. By the time the system was pumped down to a vacuum of about  $10^{-7}$  Torr, the sodium surface stopped changing appearance and remained light gray. When the sodium target was hit by the laser beam, the surface film was removed and the spot that had been struck again had a bright silvery appearance.

When the target was electrically heated, the light gray surface film grew thicker and darker. The spot that had previously been hit by the laser beam became a light gray color. The darker gray areas under this condition required 4 or 5 shots from the laser beam before their original silvery appearance could be restored. After repeated heating the sodium target began to flow and deform badly. It was apparent that there were large dimensional changes in the target and it was barely hanging in the target holder. The surface layer had become quite thick, and the surface color had become brown with a touch of yellow. The surface film had the appearance of a crust with a scaly appearance. The deformation and the flow of the target became so complete that this experiment had to be terminated.

When the target was heated, there was a detectable amount of sodium gas in the system for several minutes after the electrical current was turned off. However, the background pressures for other gases in the system also rose, and it was not possible to obtain reliable data on the laser emission after the target had been heated until the system was allowed to pump down.

Referring back to Table II-1, we see the relative effect of the active chemical nature of the sodium surface as compared to the surfaces of the targets

previously studied in the quadrupole spectrometer. We find relatively larger amounts of  $H_2O$  on the sodium surface, for example. This indicates how sodium chemically combines with water vapor from the air. A relatively large amount of hydrogen is observed. This is probably due to the decomposition of the various hydrocarbons, since we see many hydrocarbon fragments. The two groups  $CH_4$  and  $C_2H_6$  with their fragments are represented extensively in Table II-1. The largest single component identified here is mass 26,  $C_2H_2$ . There are also additional hydrocarbon groups around masses 40 and 50 due to  $C_3$  and  $C_4$  types of molecules, but we have not investigated these in so much detail as the lighter hydrocarbon fragments.

The high energy neutral molecule emission from a sodium target was also studied. This is similar to that observed from the carbon targets as described previously <sup>(4)</sup>. The major portion of the emission consisted essentially of a double spike similar to the spikes as shown in Figure III-2 of the last semi-annual report. <sup>(4)</sup> A typical example of the high energy neutral molecule emission from the sodium target is shown in Figure II-8. This shows clearly the double spike feature as mentioned above. There is also an earlier pulse which is a feature not observed on the high energy neutral molecule pulses from carbon. We have been unable to identify the nature of the first pulse satisfactorily. The upper trace of Figure II-8 shows the same train of pulses on a slower time scale. An interesting feature is that in this picture the laser double pulsed, and on the upper trace we may see the same structure consisting of an ultraviolet pulse simultaneous with the laser pulse plus the three pulses due to high energy neutral molecules, repeated again about half way through the trace.

Qualitatively, there is nothing particularly distinctive about the high energy neutral molecule emission from sodium targets. The general features are very similar to what has been described earlier for other target material, although there are persistent and interesting differences in the details. By



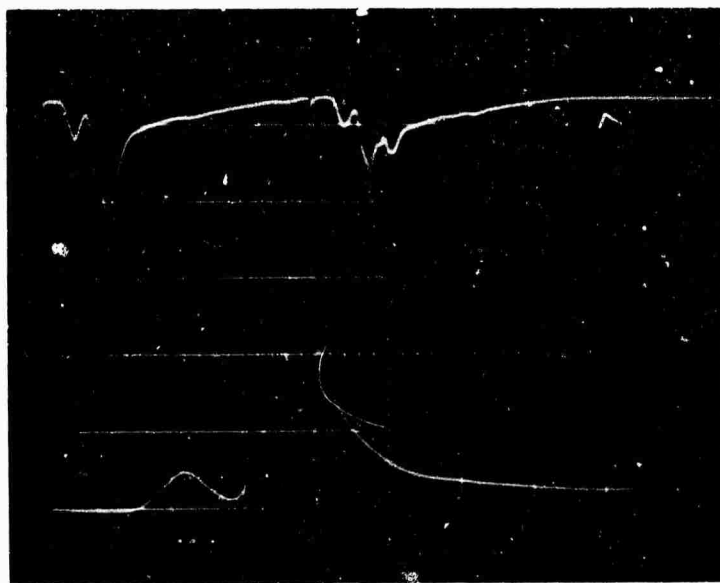


Figure II - 8 - High energy neutral molecule pulses from sodium target. Time increases from left to right. Upper trace:  $20\mu\text{s}/\text{div}$ . Lower trace:  $5\mu\text{s}/\text{div}$ . Laser power approximately 66 megawatts/cm<sup>2</sup>. Upper trace has inverted polarity. It shows the effect of second laser pulse.

taking the ratios of the arrival time of the three neutral molecule pulses as shown in Figure II-8, we find that the ratios are such that the second and third pulses are consistent with the pulses being due to CO and CO<sub>2</sub> with energies of the order of 100 eV. This is the same interpretation as arrived at for the carbon targets. However, the first somewhat lower broader pulse is troublesome in its interpretation. If this is hydrogen, the masses corresponding to the later higher spikes would be uncomfortably small. They would fall in the 8 to 12 atomic mass unit range. However, if we identify the second pulse as CO, then the mass of the first pulse would be approximately 7, which would be an unexpected value.

Figure II-9 shows data on the arrival time of the second pulse (tentatively identified above as CO) as a function of laser power per unit area. Here the variation is somewhat less than what we observed for the case of CO emitted from the carbon target, as we can see by comparing the results to those in Figure III-4 of the last semi-annual report.<sup>(4)</sup> The results shown in Figure II-9 display a considerable amount of scatter, but there is a definite trend towards decreasing values of the arrival time as the laser power per unit area increases. The numbers on the ordinate on the right hand side of the scale refer to the energies in electron volts if the mass is 28 atomic mass units. These numbers are derived from the corresponding times of flight over the distance from the target to the multiplier detector. As the laser power per unit area increases the amplitudes of the high energy neutral molecule pulses are monotonically increasing.

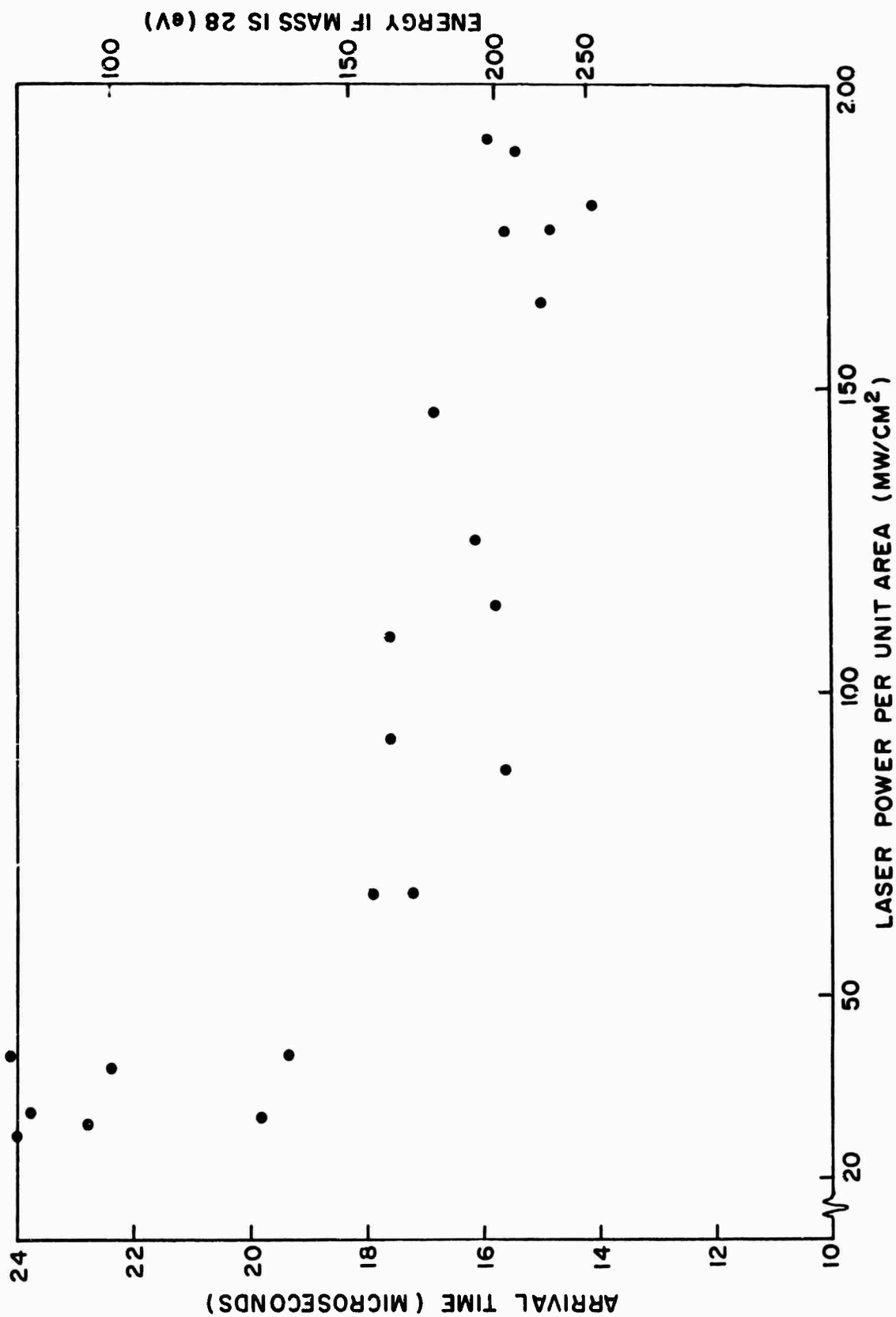


Figure II-9 - Arrival time of high energy neutral molecule pulse (second pulse in Figure II-8) as function of laser power density.

### SECTION III

#### THEORETICAL INVESTIGATIONS

##### A. ANALYSIS OF SPACE CHARGE SHEATH AND USE OF THE SAHA EQUATIONS FOR DETERMINING EXTENT OF IONIZATION IN A PLASMA

Our previous work has not considered in any detail the space charge which would be associated with the heated target surface. The purpose of the analysis in this section is to estimate the electron density in and the thickness of the space charge sheath.

Figure III-1 shows a potential diagram appropriate to the case under consideration. In the convention used here more negative potentials are shown at higher levels so that electrons tend to fall down the potential contours. The diagram (not drawn to scale) shows the Fermi level as the reference potential and point A represents the thermionic work function. Potential difference B-A is the space charge sheath of interest in this section. If there are significant numbers of positive ions a plasma is formed with the characteristic potential plateau BC. The essentially charge-free region CD indicates the potential variation due to the application of a negative potential to an electrode parallel to the target. If there were no plasma the profile would be essentially linear from points B to D.

The Richardson equation describes the outward-directed electron emission current density at a given potential relative to the Fermi level

$$J = AT^2 \exp \left[ - e (\psi_0 + \psi) / kT \right]$$

where we have expressed the potential as a sum of the thermionic work function  $\psi_0$ , and the potential,  $\psi$ , in the electron sheath. In the case where a

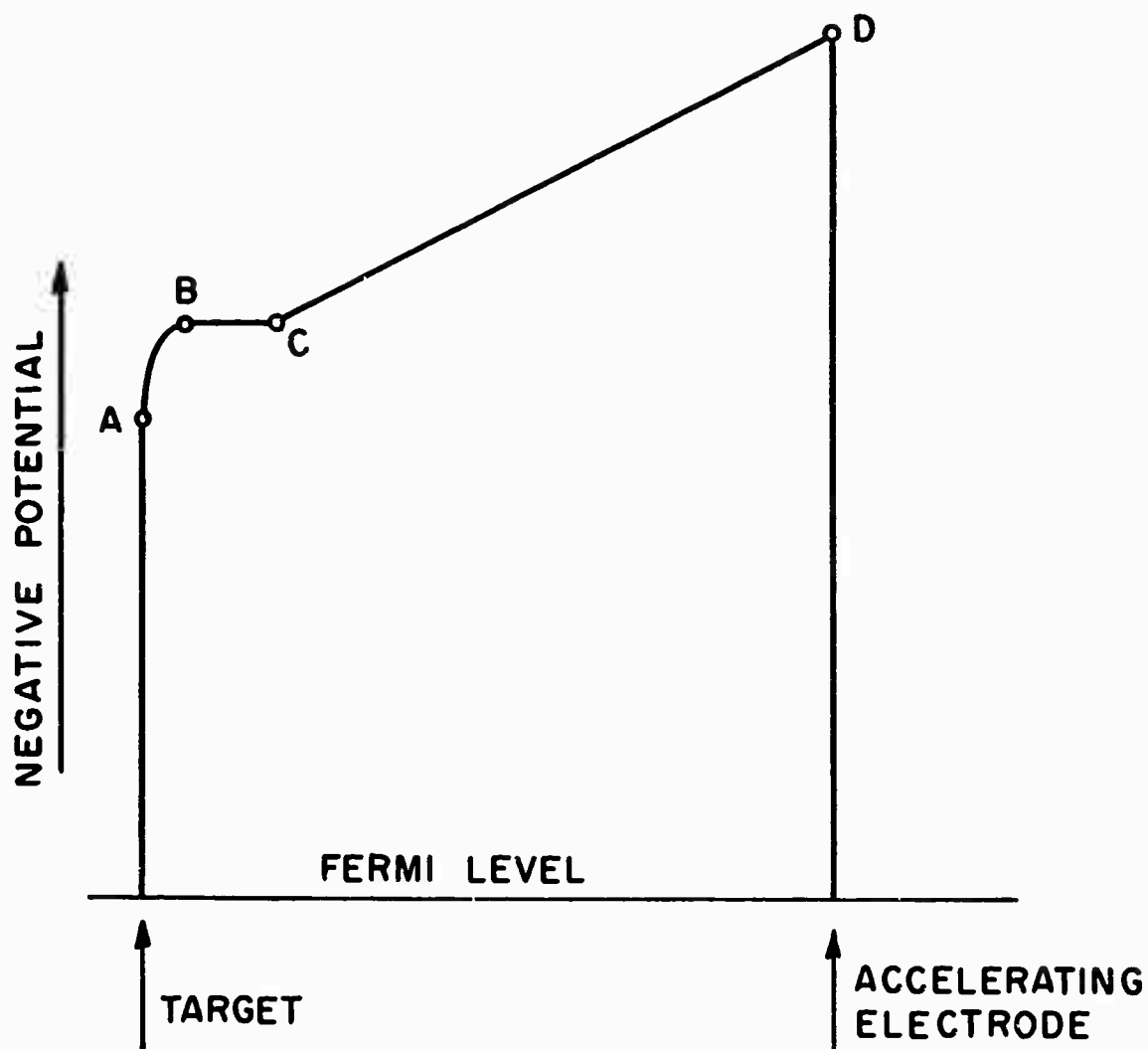


Figure III-1 - Potential diagram for a parallel plate system with emitting target and a negative potential on the second electrode.

strong ion-accelerating field is applied, essentially all the electrons will be returned to the surface or remain in the sheath. Right at the surface there will be a current density  $AT^2 \exp(-e\psi_0/kT)$  directed away from the surface and one of equal size directed toward the surface.

The distribution of the x-component of the velocity of the emitted electrons is assumed to be given by <sup>(7)</sup>

$$dN/N_0 = (m/2\pi kT)^{1/2} \exp(-m v_x^2/2kT) dv_x$$

At the surface, then, the average x-component of velocity will be given by

$$\begin{aligned} \bar{v}_x &= (1/N_0) \int v_x dN \\ &= (m/2\pi kT)^{1/2} \int_0^\infty v_x \exp(-m v_x^2/2kT) dv_x \\ &= (kT/2m\pi)^{1/2} \end{aligned}$$

The electron density at the surface would then be

$$\begin{aligned} n_e &= 2J/e\bar{v}_x \\ &= (8\pi m/e^2 k)^{1/2} AT^{3/2} \exp(-e\psi_0/kT) \end{aligned}$$

assuming the reflected electrons have the same velocity distribution as the emitted electrons. The electron density will be a maximum at the surface and decrease, roughly exponentially, as the distance from the surface increases. In the case where there was no plasma it would decrease to near zero but if there is a plasma it would decrease to the plasma density. The scale of the sheath thickness will be determined by the potential distribution in the sheath described by Poisson's equation. The extent to which any electron penetrates the sheath depends on the kinetic energy of the electron. The solution of Poisson's equation together with the equation for  $n_e$  would yield the potential and density distribution within the sheath. The

solution to this rather difficult problem is not required in detail for our purposes since the scale of the sheath thickness would be indicated by the well-known Debye length <sup>(8)</sup>

$$h = 6.9 (T/n_e)^{1/2}, \text{ in cgs units.}$$

For tungsten at 3500°K the electron density at the surface due to thermionic emission is calculated to be  $3 \times 10^{14} \text{ cm}^{-3}$  and the sheath thickness  $2 \times 10^{-5} \text{ cm}$ . It is interesting to note that as the temperature of the surface increases, the total number of electrons in the sheath will increase but that most of them will lie nearer the surface.

The above result for sheath thickness is considerably smaller than the assumption made previously <sup>(4)</sup> that the sheath dimension would be given by the electron thermal velocity multiplied by the time since emission.

Two further points should be made regarding the sheath formation. First, the largest component of the thermionic work function is due to an electron's own image force which it must overcome. <sup>(7)</sup> As indicated by the diagram in Figure III-2, the range of this force is about  $5 \times 10^{-8} \text{ cm}$  and therefore the "surface" in the analysis above is at about this distance from the physical surface. The electron density within the range of the image forces is much higher. Second, the above is a steady-state analysis. The time required to reach the steady-state would be approximately the time for an electron to travel the sheath dimension. For the example above this would be about  $3 \times 10^{-12} \text{ sec}$ .

The surface electron density, as calculated above, rises rapidly with temperature, so that high charge densities near the surface can be attained; for example,  $n_e$  reaches  $10^{17} \text{ cm}^{-3}$  at  $T = 5340^\circ\text{K}$ .

Next we will examine the use of the Saha equations for calculating the degree of ionization in a partially ionized gas or the stage of ionization (singly, doubly,

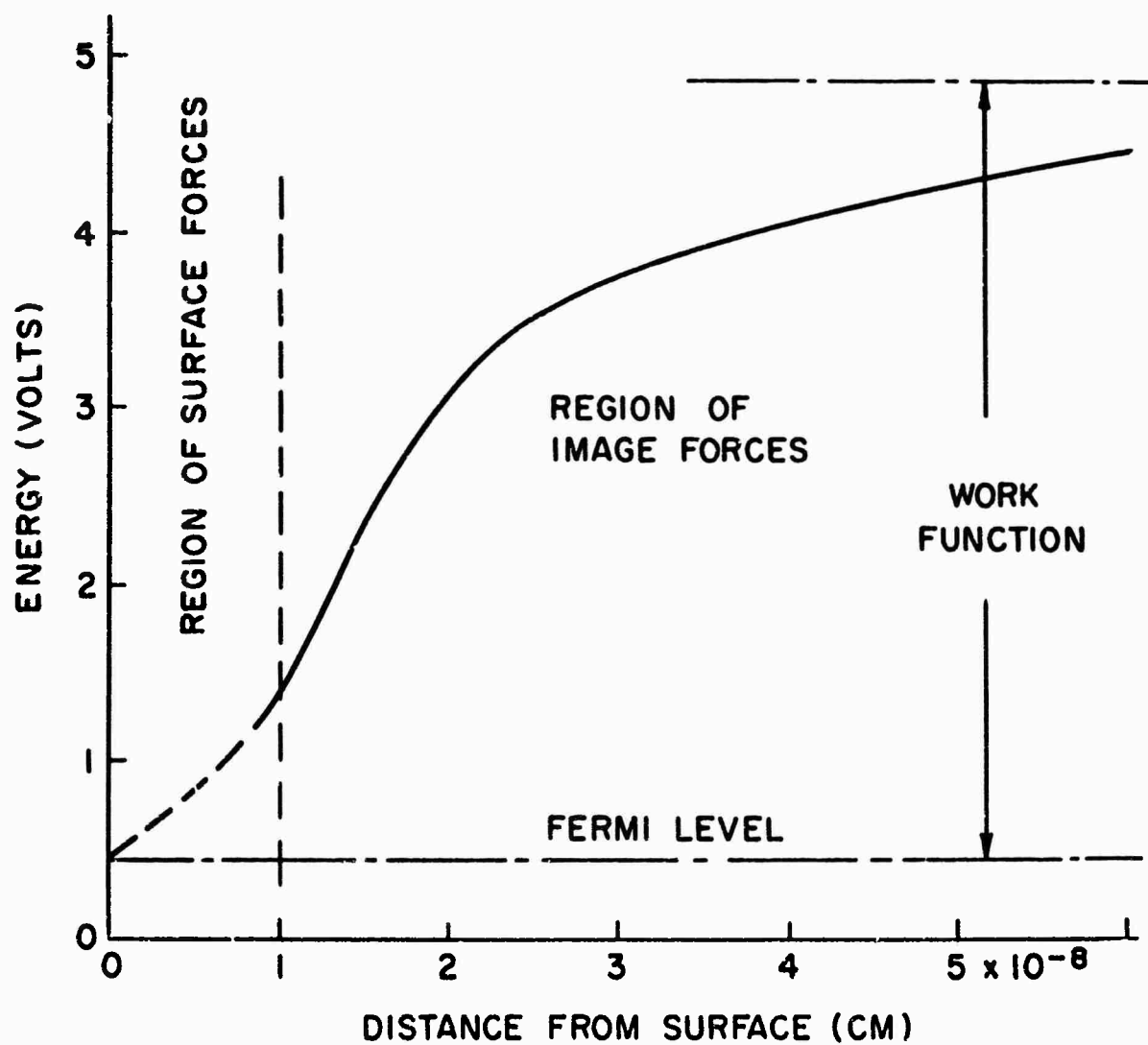


Figure III-2 - Diagram showing the energy conditions near the surface of tungsten.



triply, etc.) in a fully ionized gas. The Saha equations often predict results which conflict with our intuition, thus causing some confusion and uncertainty. The purpose of this section is to clarify what the Saha equations are and through a simple example demonstrate a rule-of-thumb which we may use in place of our intuition, should it be fallible in this case.

We are concerned here with calculating the population density in the various quantum states of a gas in thermodynamic equilibrium. The derivations are appropriate to cases of complete thermodynamic equilibrium and fortunately to cases where only local thermodynamic equilibrium (LTE) prevails. For a discussion of the conditions under which LTE prevails in laboratory plasmas, reference can be made to Griems' book.<sup>(9)</sup> Chapter 6 of this book forms the basis of the following discussion.

Figure III-3 shows a schematic energy level diagram for a certain chemical species in ionization stage  $z - 1$  ( $z = 1$  for atoms,  $z = 2$  for singly ionized ions, etc.). The ratio of densities in quantum states with energy levels  $E_n$  and  $E_m$  is given by the well-known equation

$$\frac{N_n^{z-1}}{N_m^{z-1}} = \frac{g_n^{z-1} \exp(-E_n/kT)}{g_m^{z-1} \exp(-E_m/kT)} \quad (\text{III-1})$$

where  $g_n^{z-1}$  and  $g_m^{z-1}$  are the statistical weights (the number of states at the same energy level) of the energy levels  $E_n$  and  $E_m$ . For most energy levels the statistical weights are given by the number of orientations that the total angular momentum can assume, i. e.,

$$g_n = 2J_n + 1$$

The problem now is to generalize Equation (III-1) to include the density of the free electrons associated with the ion. Referring again to Figure III-3, the

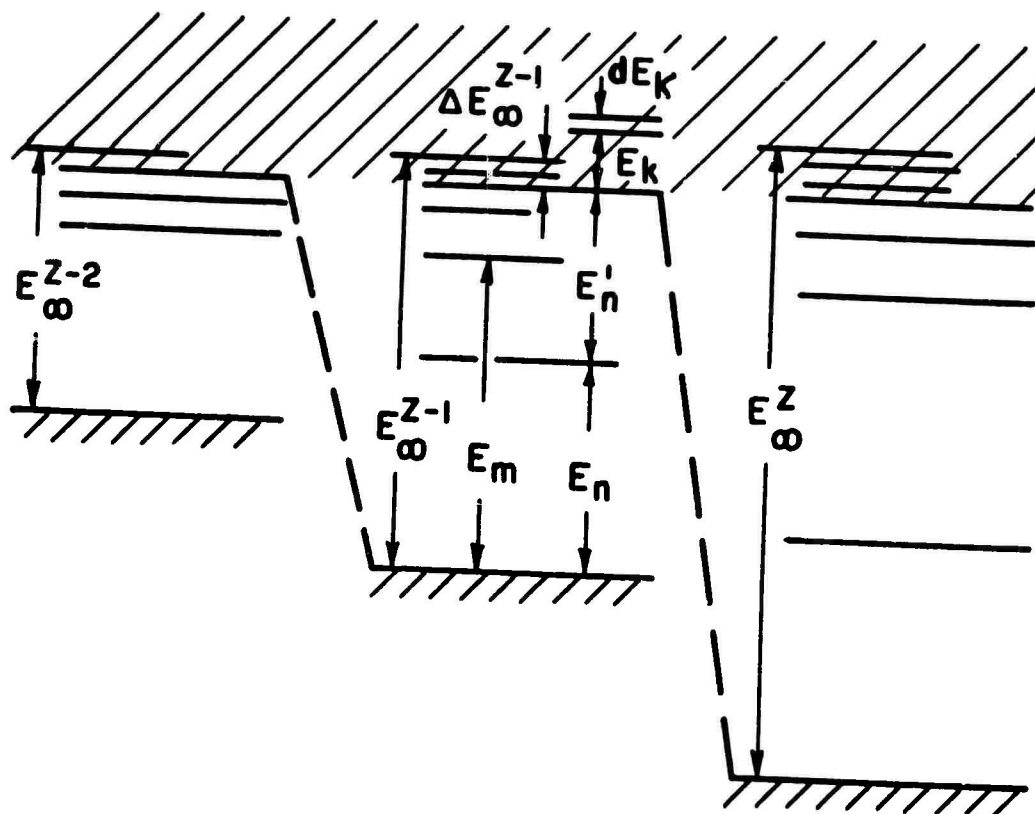


Figure III-3 - Schematic potential diagram for ions in three successive stages of ionization.

population of free electrons  $dN_e$  in the energy interval  $dE_k$  with kinetic energy  $E_k$  is given by an application of Equation (III-1) as follows:

$$\begin{aligned} \frac{dN_e}{N_n^{z-1}} &= \frac{dg_e}{g_n^{z-1}} \frac{\exp[-(E_n + E_n' + E_k)/kT]}{\exp(-E_n/kT)} \\ &= \frac{dg_e}{g_n^{z-1}} \exp[-(E_n' + E_k)/kT] \end{aligned} \quad (\text{III-2})$$

where  $E_n'$  is the binding energy of electrons in energy level  $E_n$ , and  $dg_e$  is the statistical weight of the free electron states in the energy interval  $dE_k$ . The derivation of  $dg_e$  is given by Griem. The result, in MKS units, is

$$dg_e = \frac{2g_1^z}{N_1^z} \left( \frac{E_k}{\pi} \right)^{1/2} \left( \frac{m}{2\pi\hbar^2} \right)^{3/2} dE_k \quad (\text{III-3})$$

Note that the result is in terms of the statistical weight,  $g_1^z$ , and the density,  $N_1^z$ , of the ground state of the next higher ionization stage. Let us also note here that while standard quantum-mechanical procedures are used in the derivation of Equation (III-3), it is this result which leads to the surprising predictions of the Saha equations.

Substitution of (III-3) into (III-2) and integration easily leads to

$$\frac{N_e N_1^z}{N_n^{z-1}} = \frac{2g_1^z}{g_n^{z-1}} \left( \frac{mkT}{2\pi\hbar^2} \right)^{3/2} \exp(-E_n'/kT)$$

A more useful form of the equation is the one which expresses the relationship between the total densities of two successive ionization stages and the free electron density.

$$\frac{N_e N^Z}{N^{Z-1}} = \frac{2Z^Z(T)}{Z^{Z-1}(T)} \left( \frac{mkT}{2\pi\hbar^2} \right)^{3/2} \exp \left( -\frac{E_\infty^{Z-1} - \Delta E_\infty^{Z-1}}{kT} \right) \quad (\text{III-4})$$

In this equation the  $Z(T)$  are the partition functions and are given by

$$Z(T) = \sum_n g_n \exp(-E_n/kT) \quad (\text{III-5})$$

In a plasma, the ionization energy  $E_\infty$  is reduced by a (small) amount  $\Delta E_\infty$  due to the Coulomb interaction of the plasma in which the ion is formed. This reduction in ionization potential limits the (otherwise infinite) number of terms in the sum of Equation (III-5) so the partition functions may be evaluated. The dominant term in the partition function is the statistical weight of the ground state of the configuration in question.

In the general case, for a given chemical composition (i. e., known densities of atoms and ions  $N_a$  of chemical species a) the various atom and ion densities in the plasma may be determined as a function of temperature. In addition to the Saha equations (III-4) one needs only the equations of conservation of mass,

$$N_a = \sum_Z N_a^Z$$

and macroscopic neutrality,

$$N_e = \sum_{Z, a} z N_a^Z$$

While many situations require detailed quantum-mechanical information and the use of a computer to obtain suitable solutions, we may investigate a simple situation to illustrate a point. Let us calculate the electron density as a function

of temperature for a system in which there is a total density of  $N_a = 10^{17}$   $\text{cm}^{-3}$  of carbon atoms and ions. (This is approximately equivalent to a pressure of 3 Torr at room temperature.) We will consider the problem in two temperature ranges - low temperature where ionization is not complete and high temperature where appreciable multiple ionization is achieved.

In the low temperature range of interest the partition functions for the neutral carbon atom and the singly ionized ion are given by Griem <sup>(9)</sup>, page 560,

$$Z^0 = 10.79$$

$$Z^1 = 6.07$$

These values may also be obtained directly for the case in which the temperature is not too high, so that the first few terms tend to dominate the series, simply by carrying out the summation in equation (III-5) using tabulated values <sup>(10)</sup> for  $J_n$  and  $E_n$  for the various excited states. The first ionization potential for carbon is 11.27 volts.

Expressing temperatures in electron volts and densities in  $\text{cm}^{-3}$  Equation (III-4) becomes:

$$\begin{aligned} \frac{N_e^2}{N_a - N_e} &= 4.21 \times 10^{21} T^{3/2} \exp(-11.27/T) \\ &= F(T) \end{aligned}$$

In the region of interest  $4N_a/F(T) \gg 1$  and therefore

$$N_e \approx [N_a F(T)]^{1/2}$$

A plot of this equation is shown as part AB of the curve in Figure III-4. At temperatures above about 1 eV there is significant multiple ionization. In the

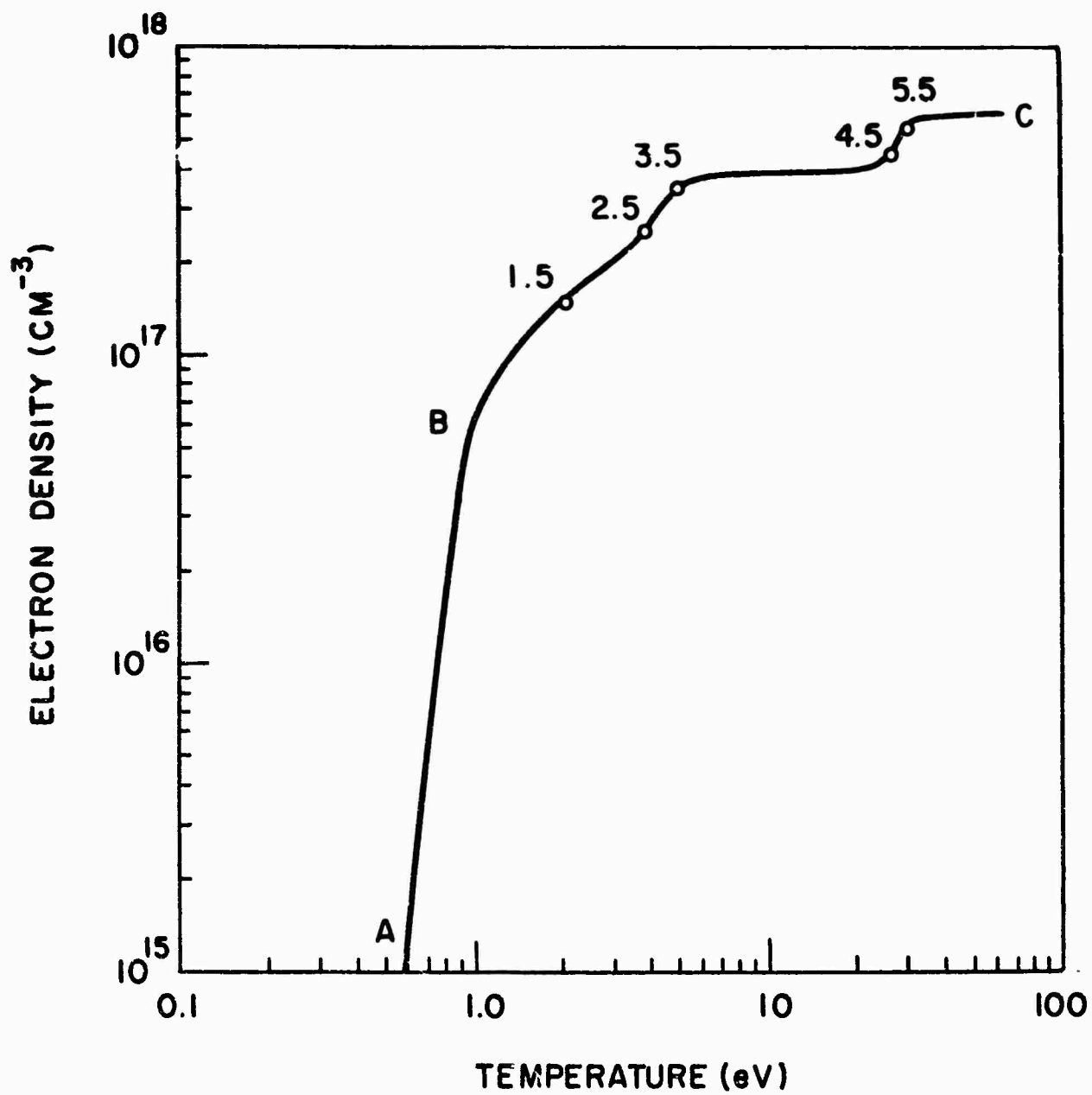


Figure III-4 - Equilibrium electron density as a function of temperature for carbon nuclei density of  $10^{17} \text{ cm}^{-3}$ .

high-temperature region we calculate the temperature  $T^{z-1/2}$  where  $N^{z-1}$  and  $N^z$  are equal. ( $N^{z-2}$  and  $N^{z+1}$  will be small in comparison.)

First we see that

$$N_e = (z-1/2) N_z$$

If we neglect the correction  $\Delta E_\infty^{z-1}$  and take the ratio of the partition functions of successive stages of ionization to be unity (assumptions which will have little affect on our result) then Equation (III-4) becomes

$$(z-1/2) = 7.5 \times 10^4 (T^{z-1/2})^{3/2} \exp(-E_\infty^{z-1}/T^{z-1/2})$$

for a total carbon density of  $10^{17} \text{ cm}^{-3}$ . The ionization potentials  $E_\infty$  for carbon are tabulated in Table III-1 along with the corresponding solutions for  $T^{z-1/2}$ .

TABLE III-1  
IONIZATION OF CARBON

$z$	Ionization Potential (volts)	Stage of Ionization ( $z-1/2$ )	$T^{z-1/2}$ eV
1	11.26	-	-
2	24.38	1.5	2.1
3	47.86	2.5	3.9
4	64.48	3.5	5.1
5	391.99	4.5	27
6	489.84	5.5	31

The results of this calculation are shown as points labeled 1.5, 2.5, etc. in Figure III-4. The curve through these points would approximate the electron density curve in the plasma.

We see that the gas becomes essentially fully ionized when the electron temperature is about 1 eV and the atoms are completely stripped of the orbiting electrons when the electron temperature approaches 40 eV. A good rule-of-thumb is that the electrons with a given electron temperature (and LTE at least prevails) will cause ionization of levels up to about an order of magnitude higher in energy.

Physically the ionization comes about through two effects:

- 1) There are some high energy electrons in the electron energy distribution with enough energy to move an electron from the ground state to a free state.
- 2) Most of the ionization would occur, however, as the result of a multi-step process wherein the bound electron is moved through successively higher excited levels until it is finally free.

That the equilibrium populations are as indicated by the equations and not as one might guess, however, is because of the high statistical weight of the free-electron states.

These considerations about the ionization level and the depth of the layer in which the electronic charge is concentrated lead to revised values for the charge densities near the surface, and hence to different plasma heating rates, than were employed in our earlier consideration of plasma heating.<sup>(2)</sup> The problem of plasma heating must be reviewed in the light of the preceding paragraphs. We will see that for the present at least we must leave open the possibility that the plasma heating is due to the inverse bremsstrahlung process.

The plasma heating calculation<sup>(2)</sup> took the electron density as a variable independent of the ion density. The indication that the space charge sheath is



relatively small suggests that except where consideration is specifically restricted to the sheath region, macroscopic charge neutrality should be taken as a boundary condition. This would alter somewhat the use of the Saha equations in the earlier calculations.

The previous calculations also assumed thermodynamic equilibrium in the electron-ion-neutral system although it was pointed out that the heating would go from electrons to ions to neutrals. It was shown in an earlier report <sup>(2)</sup> that even the transfer of energy from electrons to ions was slow enough to cause some concern regarding the equilibrium assumption. The heating of the neutrals would lag further behind.

It should be pointed out that thermodynamic equilibrium is not necessarily required in order to correctly use the Saha equations. Local thermodynamic equilibrium (LTE) is a sufficient condition and in laboratory plasmas when electron-ion collisions dominate the rate processes then LTE prevails. Situations can arise then in which ions can be multiply ionized due to hot electrons but the ion themselves can remain relatively cool.

In view of this it opens the possibility of eliminating all the un-ionized blow-off material from the plasma heating system and considering separately the transfer of energy from the electrons to the ions. The problem can then be divided into two parts: first describing the manner in which the plasma electrons absorb energy from the laser beam and then how the energy is transferred from the electrons to the ions in amounts indicated by the experimental observation of ion energy.

The model suggested by this reasoning is then that the plasma in front of the target would be formed by (predominantly alkali metal) ions which were emitted from the target in the ionized state and thermionically generated electrons. The electrons would absorb energy from the laser beam and subsequently transfer some of it to the ions. Only preliminary estimates have been made using this model at this time. The calculations will be refined further in the next report period.

## B. CALCULATION OF LASER-INDUCED PRESSURE PULSES IN THE TARGET

The absorption of laser radiation at a surface can produce large pressure waves in the target material. This phenomenon is of considerable interest. One mechanism by which pressure pulses could be produced would be evaporation of material from the surface with subsequent heating of the material and recoil of the heated material against the surface. A considerable amount of work on this phenomenon has been done previously.<sup>(11)</sup> Some work on experimental measurement of the pressure pulses obtained in this way in comparison with a model similar to that of Pyatt<sup>(11)</sup> has also been reported.<sup>(12)</sup> This work has mainly been carried out at high laser power per unit area where a considerable amount of material is removed from the surface.

There is also another mechanism by which laser produced pressure pulses can be generated. This does not involve removal of any material from the surface and can occur at considerably lower laser power per unit area. This effect can be termed a thermomechanical effect. As the laser radiation is absorbed in a thin layer near the surface, the internal energy of that layer increases. This heated layer will expand by thermal expansion. If the heat is absorbed slowly, the expansion can take place in such a way that adjacent layers of material can relax and no shock wave will be generated. In other words, the adjacent layers of material have time to move out of the way. An ordinary thermal expansion of the material will occur. If, however, the thermal energy is deposited in a thin layer in a very short time, that is, in a time much shorter than the relaxation time for the adjacent material, a pressure wave can be generated. The heated material is trying to expand before the adjacent material can relax and allow it to expand. Thus, a pressure is generated on the adjacent material.

A rough estimate of the time in which the surrounding material can relax can be obtained from the following consideration; relaxation time equals thickness of the layer divided by the speed of sound in the material, since the

relaxation which would produce relief of the pressure pulse is propagated by phonons which travel at the velocity of sound. For laser-heated surfaces the amount of material involved is of the order of  $10^{-4}$  cm thick if one includes thermal conduction. The velocity of sound is of the order of  $10^5$  cm/sec. Thus, if a significant amount of heating is experienced in a time shorter than  $10^{-9}$  seconds, there will be insufficient time for the relaxation to occur and the heated material will be trying to expand against the surrounding layers. Thus, a pressure pulse will be produced. If the scale of heating is long compared to  $10^{-9}$  seconds, relief of the pressure can be obtained during the time of the pulse and we would expect no shock wave.

This effect is of interest in an investigation of effects of laser radiation. Accordingly, we have carried out calculations on the magnitude and time history of pressure pulses produced in our experimental situation. The analytical tool used for these calculations was the PUFF computer code. PUFF is a one-dimensional Lagrangian program which has been used previously in the study of X-radiation effects. The program was generated at the Air Force Weapons Laboratory in Albuquerque.

The PUFF code uses finite difference methods to solve the hydrodynamic equations using a slab geometry and assuming one-dimensional flow. One may follow a pressure pulse moving through a sample consisting of a number of separate materials. The number of different materials may be chosen as an input variable and may be an integer between 1 and 6. A grid or mesh is superimposed on the materials in the sample. The grid areas are called zones, and the grid lines are called zone boundaries. The mesh is numbered increasing from left to the right. The radiation is considered as being incident from the left, and the pressure pulse starts from the left and progresses through the mesh to the right. The main PUFF program is used as a control program to call various subroutines which carry out specific portions of the calculation. There are six subroutines called GENRAT, HYDRO, REZONE, EDIT, EQST, and SSCAL.

GENRAT is called once at the start of a problem, and reads the input data and calculates the energy deposition in the material. The hydrodynamic calculations are carried out in the subroutine HYDRO. HYDRO calculates propagation of a pressure pulse through the mesh of zones by a finite difference method. Starting with the left zone and with the initial conditions at the beginning of the problem, the zone velocity, the position of the zone boundary, and the pressure in the zone are calculated. Then the same quantities are calculated for the next zone using as boundary conditions the new pressure in the preceeding zones. These variable by variable, zone by zone, calculations continue until all zones have been advanced to a new time. This is one cycle of the program. Then starting with the state of the material at the new time, the same variables zone by zone at an incremented time are recalculated. Thus, working cycle by cycle, a stress history of the shock wave in the material as a function of depth and time is obtained.

Since available computer time limits a problem to a few hundred zones, the REZONE subroutine distributes the zones where they are most needed by reducing the zone sizes in the main pressure pulse and increasing the zone sizes in less active regions of the mesh. The criterion used is that the zone sizes are made smallest where the pressure gradient is largest. The EDIT subroutine is used to output a number of key quantities at designated intervals during the program. The SSCAL subroutine calculates the increase in internal energy in each zone due to absorption of energy from the laser beam during the incremented time between cycles. The EQST subroutine calculates the equation of state of the material from which the pressure as a function of other variables is obtained. The general flow of the problem is shown in Figure III-5.

It is not the purpose here to describe all characteristics of the PUFF computer program in detail. Details may be found in an AFWL technical report.<sup>(13)</sup> However, it is worthwhile to devote a little discussion to the pressure calculations carried out in PUFF. PUFF is an elastic-plastic program. In other words,

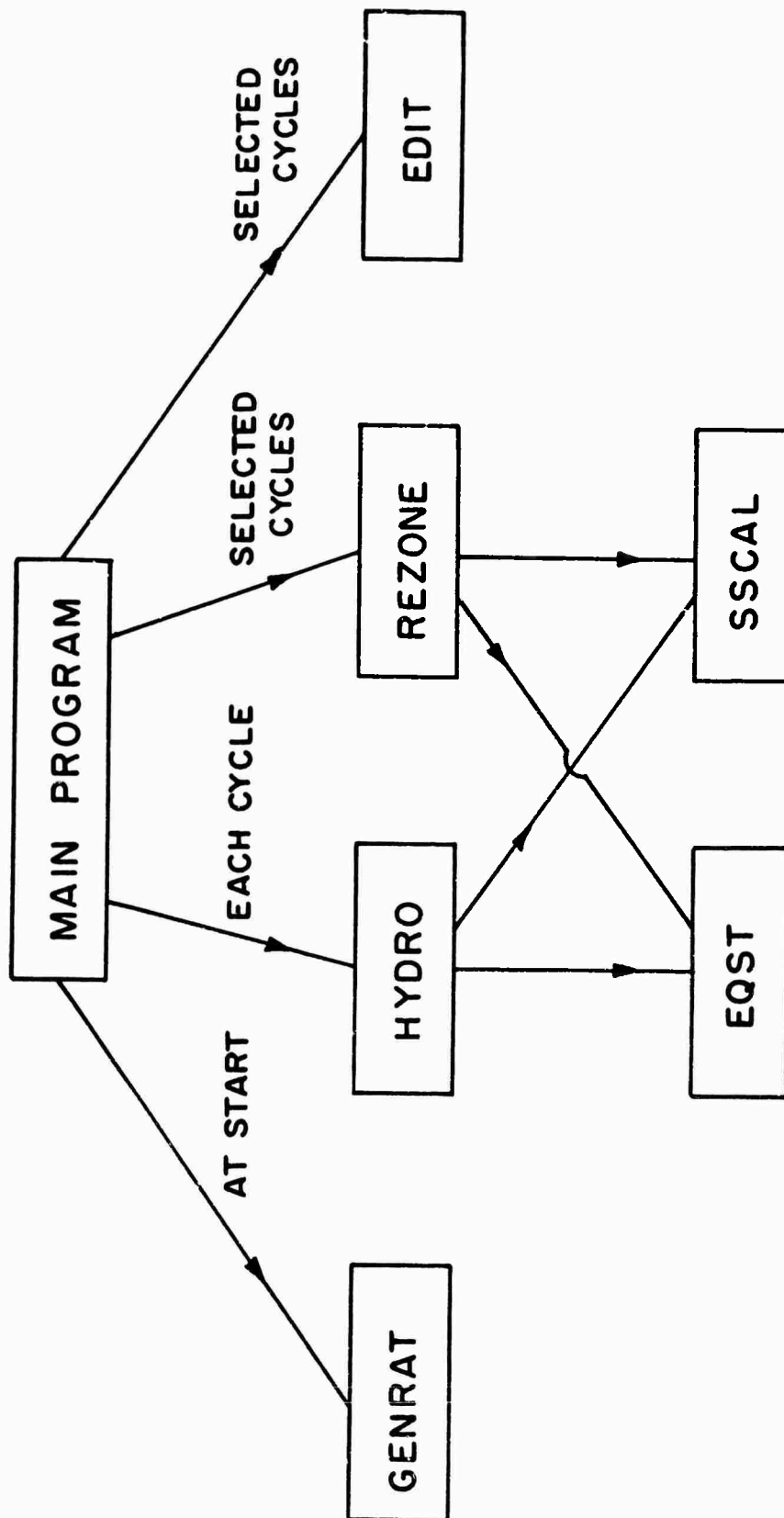


Figure III-5 - Flow of PUFF Code

for pressures below the elastic limit it is assumed that the material deforms elastically, and when the pressure is released the material returns to its original undistorted state. When the yield strength of the material is exceeded, however, plastic work is done on the material and the material is permanently deformed. Doing the plastic work extracts energy from the pulse so the pressure pulse is attenuated by passage through the material.

One must be cautious to choose values for the input mechanical properties of the material that reproduce wave propagation experiments. The equation of state that appears in PUFF is of the form:

$$P = (C\mu + D\mu^2 + S\mu^3) (1 - G\mu/2) + G_0 E$$

Here  $P$  is the pressure,  $C$ ,  $D$ , and  $S$  are input parameters that must be matched to wave propagation experiments and are characteristic of a particular material,  $G$  is the Gruneisen ratio of the material,  $\mu$  is the compression of the material,  $\mu = \rho/\rho_0 - 1$ ,  $\rho$  is the density of the material at the current time and position, and  $\rho_0$  is the original uniform density of the material, and  $E$  is the internal energy. This equation of state is matched to Hugoniot which is obtained from shock wave data. Such data may be obtained in the literature<sup>(14)</sup> where shock wave data have been projected to the  $P$ - $\mu$  plane and the fitting has been done to obtain values for  $C$ ,  $D$ ,  $S$ , and  $G$  for various metals.

Modifications in the PUFF code were necessary to suit the problem to our particular application. The two main modifications were the use of experimental absorption coefficients characteristic of the monochromatic laser light, and changing the input and output statements in the program to be compatible with an H-1800 computer. The PUFF code was originally designed to handle a broad spectrum of X-radiation as input. The absorption coefficients are based on the formula:

$$(\mu/\rho)_i = A_i(E)^{B_i}$$

where  $\mu/\rho$  is the mass absorption coefficient,  $i$  refers to the interval between the  $i^{\text{th}}$  and  $(i+1)^{\text{th}}$  absorption edges of the material,  $E$  is the photon energy, and  $A_i$  and  $B_i$  are constants for the given interval for the given material. Between two absorption edges  $\ln(\mu/\rho)$  is a linear function of  $\ln E$ . This treatment handles the absorption coefficient very well at X-ray energies less than the K-absorption edge, and it is also capable of handling input radiation with a broad energy spectrum. However, for our particular problem it does not give a good picture of the deposition of monochromatic light at optical frequencies.

Accordingly, we modified the program by removing the entire section of the GENRAT subroutine where the absorption coefficient is calculated and inserting statements to accept experimental values of the absorption coefficient directly as input data. Choice of the appropriate values for these input parameters poses a problem in that, during the scale of time we are interested in, the input energy is conducted by thermal conduction from the layer of material in which it is originally absorbed to a greater depth. In our first attempt to use the code, we used the raw data for optical absorption coefficients at the ruby laser wavelength. Later, for reasons to be discussed below, we modified the values of the input absorption coefficient to use effective absorption coefficients that account for conduction of heat in the materials, since PUFF makes no provision for thermal conduction. In the case of X-radiation, for which PUFF was designed, this makes no difference since the X-rays are absorbed over a scale of depths such that thermal conduction is negligible. For our case heat conduction becomes important as we shall see later.

At this point we made a few trial runs of the PUFF code using as input for the absorption coefficient values of the optical absorption coefficient for ruby laser light. These computer runs gave sharp pressure pulses that propagated from the surface of the material to the interior. The results appeared to be physically reasonable. However, there was a considerable problem in zoning.

The original zone size is introduced as an input variable. A necessary feature to get physically meaningful results is that the original zone size be small compared to the depth over which the radiation is absorbed. Each zone must absorb only a small fraction of the radiation incident on its front surface. Since the absorption coefficients for optical radiation are very large compared to those for X-rays, the zones must be much smaller for an optical problem as compared to an X-ray problem. This means a large number of zones and, since each zone has all its variables calculated in each cycle of the problem, this means that the running time for the program becomes unreasonably long.

The solution to this problem comes from considering the fact that heat is actually conducted by ordinary thermal conduction a distance that is large compared to the inverse of the optical absorption coefficient even in times of the order of nanoseconds.<sup>(15)</sup> Thus, we can define an effective absorption coefficient which is the inverse of the depth to which the energy is actually distributed during the time of the laser pulse, considering both the depth over which it is originally deposited and the depth to which it is conducted during the pulse duration. This absorption coefficient can be considerably smaller than the original raw optical absorption coefficient.

With this formulation we attained meaningful results that are summarized in Figure III-6. Each curve in the figure represents a pressure profile as a function of depth at a particular time after the start of the laser pulse. We see that for approximately 1 nanosecond the height of the pressure pulse keeps increasing. At that time the position of maximum amplitude begins to move toward the right through the material at approximately the speed of sound. The amplitude no longer builds up, but instead gradually decreases as the pressure pulse moves to greater depths. As a function of depth, we see that we get a very sharp pressure pulse propagating through the material. The particular sample chosen here was taken as  $70\mu$  thick. This particular choice of thickness is not important to the results since the pressure pulse would merely continue to propagate if the material were thicker, gradually being attenuated as it went to greater depths in the material.



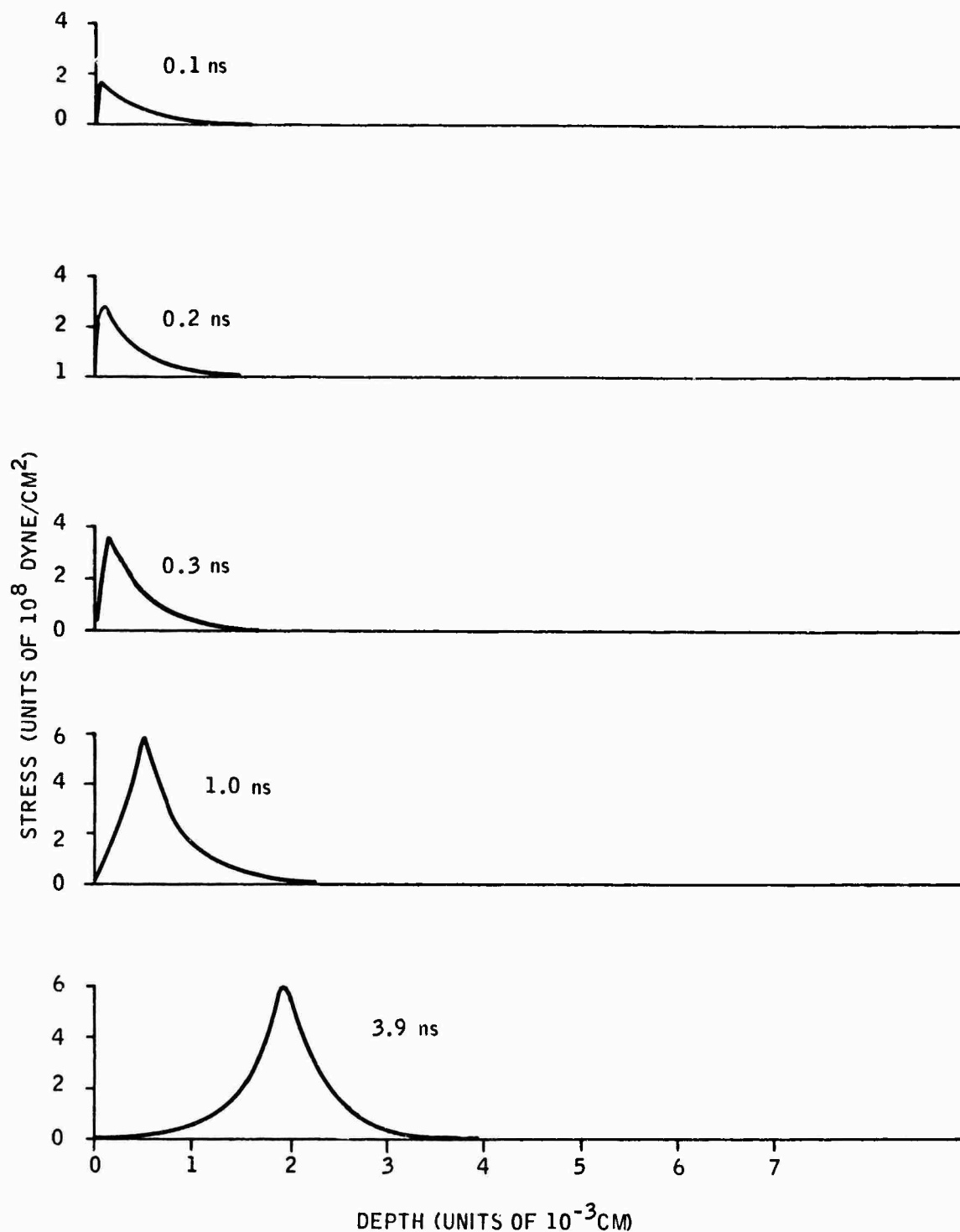


Figure III-6 - Stress profiles as a function of depth in tungsten target struck by a flat laser pulse depositing  $0.3 \text{ cal/cm}^2$  in 30 nanoseconds as calculated by the PUFF code. Each profile represents a different time after the start of the laser pulse.

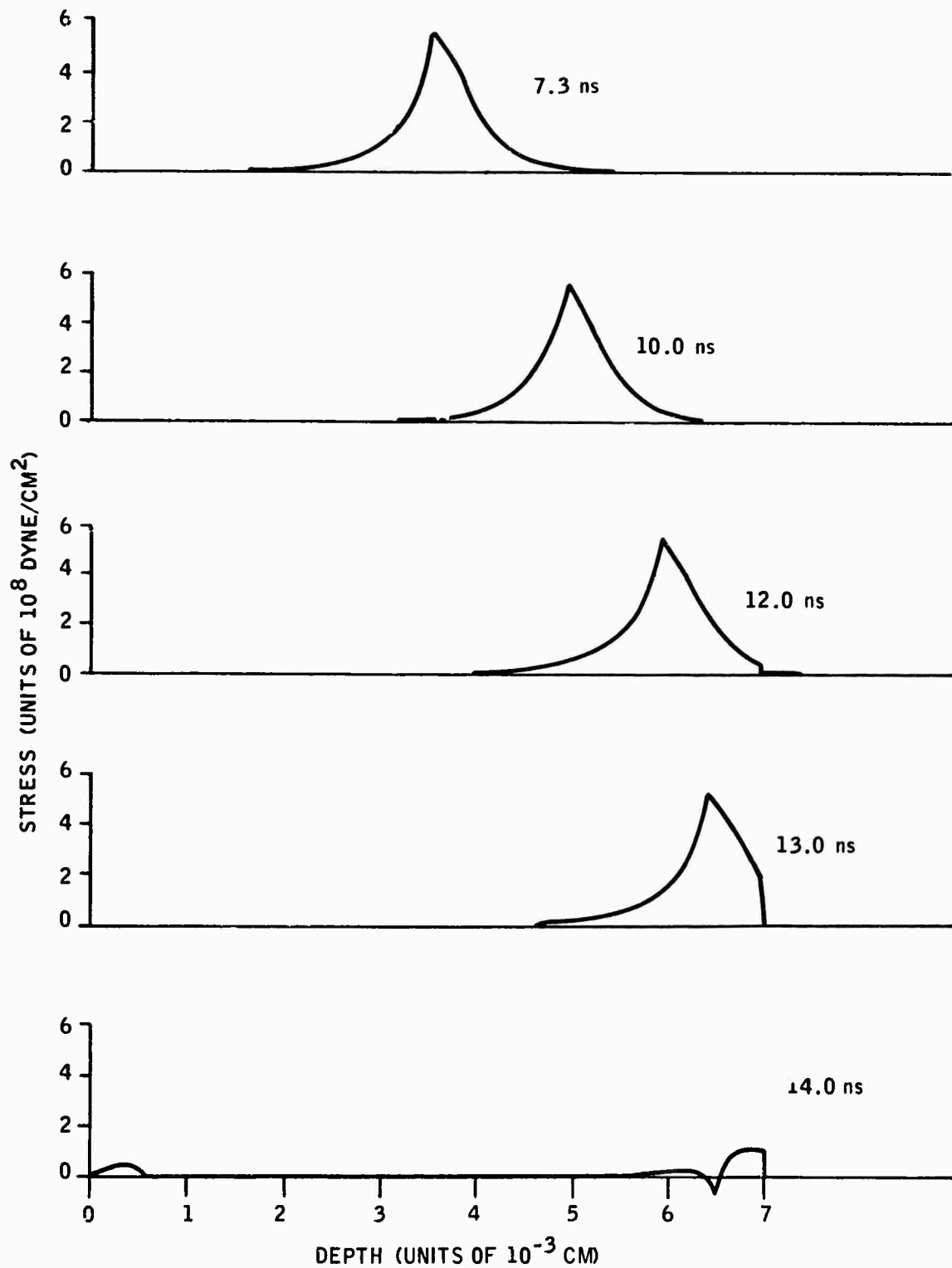


Figure III-6 - (Continued) - Stress profiles as a function of depth in tungsten target struck by a flat laser pulse depositing  $0.3 \text{ cal/cm}^2$  in 30 nanoseconds as calculated by the PUFF code. Each profile represents a different time after the start of the laser pulse.

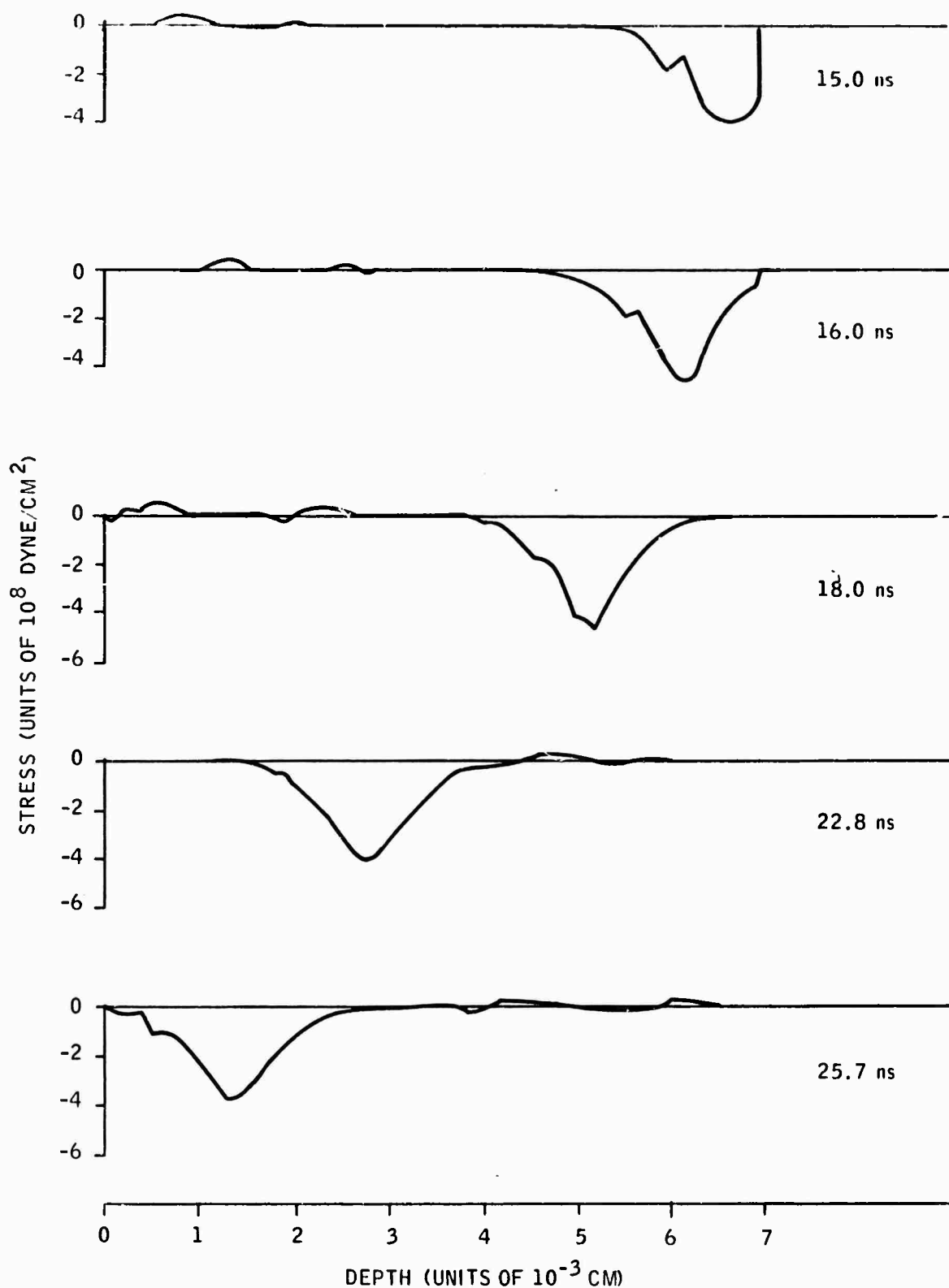


Figure III-6 - (Continued) Stress profiles as a function of depth in tungsten target struck by a flat laser pulse depositing  $0.3 \text{ cal/cm}^2$  in 30 nanoseconds as calculated by the PUFF code. Each profile represents a different time after the start of the laser pulse.

Around 15 nanoseconds after the start of the laser pulse the pressure wave reaches the rear surface of the material. There it is reflected as a tension wave. If this tension wave is large enough, it can exceed the ultimate tensile strength of the material and cause spallation at the back surface. The tension wave moves back into the material, propagating toward the left. At the front surface it would again be reflected as a positive compression wave which would move from left to right. This pressure pulse would bounce back and forth a number of times between the surfaces until it gradually damped out. The laser energy per unit area integrated over the pulse in this case was chosen to be  $0.3 \text{ cal/cm}^2$  in a flat pulse of 30 nanosecond duration. These values are characteristic of pulses used in our experiments. The temperature at the tungsten surface would increase by about  $1350^\circ\text{C}$  because of absorption of such a pulse, so that we would not be in a region where vaporization is important. We see that the peak value of the pressure is of the order of  $6 \times 10^8 \text{ dynes/cm}^2$ . By comparison the yield strength of tungsten is approximately  $1 \times 10^{10} \text{ dynes/cm}^2$ , and the ultimate tensile strength of tungsten is approximately  $3 \times 10^{10} \text{ dynes/cm}^2$ . Thus for our case we should have only an elastic deformation and we would expect no spallation to occur at the back surface of the material. As the laser power per unit area is increased, we expect this conclusion would be changed. First, as the maximum stress became larger than the yield strength, permanent deformation would occur, and as the laser power per unit area increased still further, we would expect the possibility of scabbing of the back surface of the thin slab as the ultimate strength of the material was exceeded.

The dominant feature is the large single stress wave moving to the right through the material. The speed of sound is calculated to be approximately  $.4 \times 10^6 \text{ cm/sec}$ . The duration of the laser pulse is 30 nanoseconds but the maximum amplitude of the stress wave stops increasing relatively early in the laser pulse. In fact, the maximum amplitude is reached around 1.0 nanoseconds after the beginning of the laser pulse. At this time the maximum

stress is  $5.87 \times 10^8$  dynes/cm<sup>2</sup>. The position of the maximum stress is at approximately .0005 cm from the left edge. Previous to this time the maximum amplitude of the stress has been increasing steadily as the stress wave moves to the right. After this time the amplitude of the stress wave increases only slightly and then goes into a gradual decline. The attenuation as the stress wave passes through the material is to be expected. Since the maximum stress does not exceed the yield strength of the material, no plastic work is done, and we would expect the wave to be attenuated only slowly by the gradual expansion of the entire slab of material. This in fact is observed. Around 15 nanoseconds the stress wave reaches the rear surface and is reflected with about a 20% decrease in amplitude. Thereafter it propagates to the left as a rarefaction wave.

A surprising feature of this whole process is that there is no succeeding stress wave produced by absorption of energy at times greater than 1 nanosecond. Very early in the laser pulse the maximum stress is achieved and thereafter the left surface of the material remains approximately at zero stress until the rarefaction wave returns. There is, of course, some question as to whether this might possibly be an artifact of the hydrodynamic program. We have considered this question carefully and have come to the conclusion that this represents the true behavior, at least the true behavior of the hydrodynamic model used in PUFF. The reason that the stress wave stops increasing in amplitude after approximately 1 nanosecond is that the position of the maximum amplitude has moved out of the region where the energy is being deposited, at least for a flat pulse. This would probably be different if a triangular pulse shape were used. At the depth of .0005 cm, where the amplitude stops increasing, the energy deposition integrated over the entire laser pulse is approximately  $.45 \times 10^8$  ergs/gram, or about one quarter of what it was at the surface. As the stress wave propagates to deeper depths it does indeed increase very slightly, but it is passing through a region where the rate of energy deposition has become very low. On the other hand, to the left of the position where the maximum amplitude occurs, we can observe that the hydrostatic pressure

does indeed continue to increase with time as further laser energy is deposited in these regions. The deposition of energy leads to an increase of the hydrostatic pressure through the equation of state subroutine. However, from a detailed examination of the profiles we deduce that the stress to the left of the position of the maximum is near zero even though the hydrostatic pressure is large. The reason for this is that the hydrostatic pressure is almost exactly balanced off by a negative deviatoric stress. The deviatoric stress measures the stress produced by the expansion of the material. The deviatoric stress is calculated in the HYDRO subroutine and is a function of the expansion of the material and the velocity with which it is moving. The deviatoric stress is a relief of the hydrostatic pressure by motion of the material.

Thus a physical picture of the processes occurring is that at the very beginning of the laser pulse when the material is at rest and in its uncompressed state the deposition of energy begins to produce a stress which is relieved by expansion at the left edge of the material. Later when the material is already expanding fairly rapidly, the expansion relieves the stress produced by the increment of the deposited energy rapidly enough so that there is no net stress in the material. It must be remembered that for these runs the total stresses are relatively low compared to the ultimate strength of the material. We nowhere exceed the yield strength of the material which is taken to be approximately  $1 \times 10^{10}$  dynes/cm<sup>2</sup>. This situation is different when larger amounts of energy are deposited and where the maximum stress will begin to approach the yield strength of the material. In that case the stress can no longer be relieved rapidly enough near the left edge of the material.

An interesting feature of this result is that the stress profile is relatively independent of the laser pulse after the first nanosecond. Thus, we should expect at the rear surface shock waves of approximately the same amplitude and duration even if we were to cut off the end of the laser pulse. That is, a

laser pulse of one nanosecond duration should produce the same shock wave at the rear surface as a laser pulse of 30 nanosecond duration, provided the power per unit area delivered by the two pulses is the same, and the peak stress is less than the yield strength. This prediction could be investigated experimentally by using high frequency pressure transducers in contact with the rear surface of the sample. This also means that the artifact of introducing details in the thermal conduction process does not have a great effect on the stress wave profile, as we shall see below. This occurs because the stress wave propagates out of the region where energy is being conducted quite early in the pulse and the thermal conduction will occur only in the region where the stress wave has been relieved and where the relief processes are keeping up with the increase in hydrostatic pressure during the subsequent portion of the pulse.

An alternative way of looking at this is to consider the time for a stress relief wave to be propagated across the layer where energy is being deposited. Stress relief propagates at the speed of sound in the material, leading to a characteristic time of around one nanosecond, as we saw previously. This is in fact the length of time after which the stress stops increasing in amplitude. Since the stress in the layer in which the energy was deposited is relieved by expansion of that layer, and therefore a pressure is exerted against the next layer, we expect the stress to propagate into the material, rather than dropping to zero.

Some light has also been shed on this process by carrying out PUFF code runs for larger incident powers per unit area. If the power per unit area is increased, the increase in the peak amplitude of the stress wave increases approximately linearly with the increase in laser power per unit area, up to the point where the maximum stress amplitude is equal to the yield strength of the material. The shape and time history of the pressure pulse remain unchanged up to this point. As the yield strength of the material is exceeded, the maximum pressure in the sharp pulse continues to increase, but the time history changes markedly. The first sharp pulse is followed by other broader pulses of larger amplitude. The first sharp

pulse still propagates from left to right in the material as previously, but now the amplitude damps considerably faster at larger depths. We interpret this as being due to extraction of energy from the pulse to produce plastic work on the material. The later succeeding stress waves that also propagate into the material are rather complicated and we interpret these as caused by the material near the surface being strained past its elastic yield point, and thus no longer relaxing fast enough to relieve this pressure pulse. Thus, as the laser energy is raised enough so that the elastic limit of the material is exceeded by the stress wave, the time history becomes considerably more complicated. We have not pushed the investigation of the details of these phenomena to the point where we feel we can completely understand them.

An alternative way of presenting the results of the PUFF code program is shown in Figure III-7 where we present the stress as a function of time at the rear surface of a  $70\mu$  thick specimen of tungsten which is struck by a laser power of  $0.3 \text{ cal/cm}^2$  at the front surface. For approximately 8 nanoseconds there is no buildup of pressure; then a positive pressure is experienced as the compression wave reaches the rear surface. Around 15 nanoseconds after the start of the laser pulse a sharp tension pulse occurs at the back surface as the original compression pulse is reflected as a tension wave. This is the time at which scabbing of the back surface would occur if the tensile stress were to become high enough. After this time the stress drops to a relatively low value. At a later time when the tension wave is reflected from the front surface and returns to the back surface, with a relatively short period of high negative stress.

It should be noted that PUFF is a one-dimensional computer code. The conditions of applicability here are that the transverse dimensions of the laser spot should be much larger than the thickness of the foil we are considering; otherwise the one-dimensional approximation will break down.



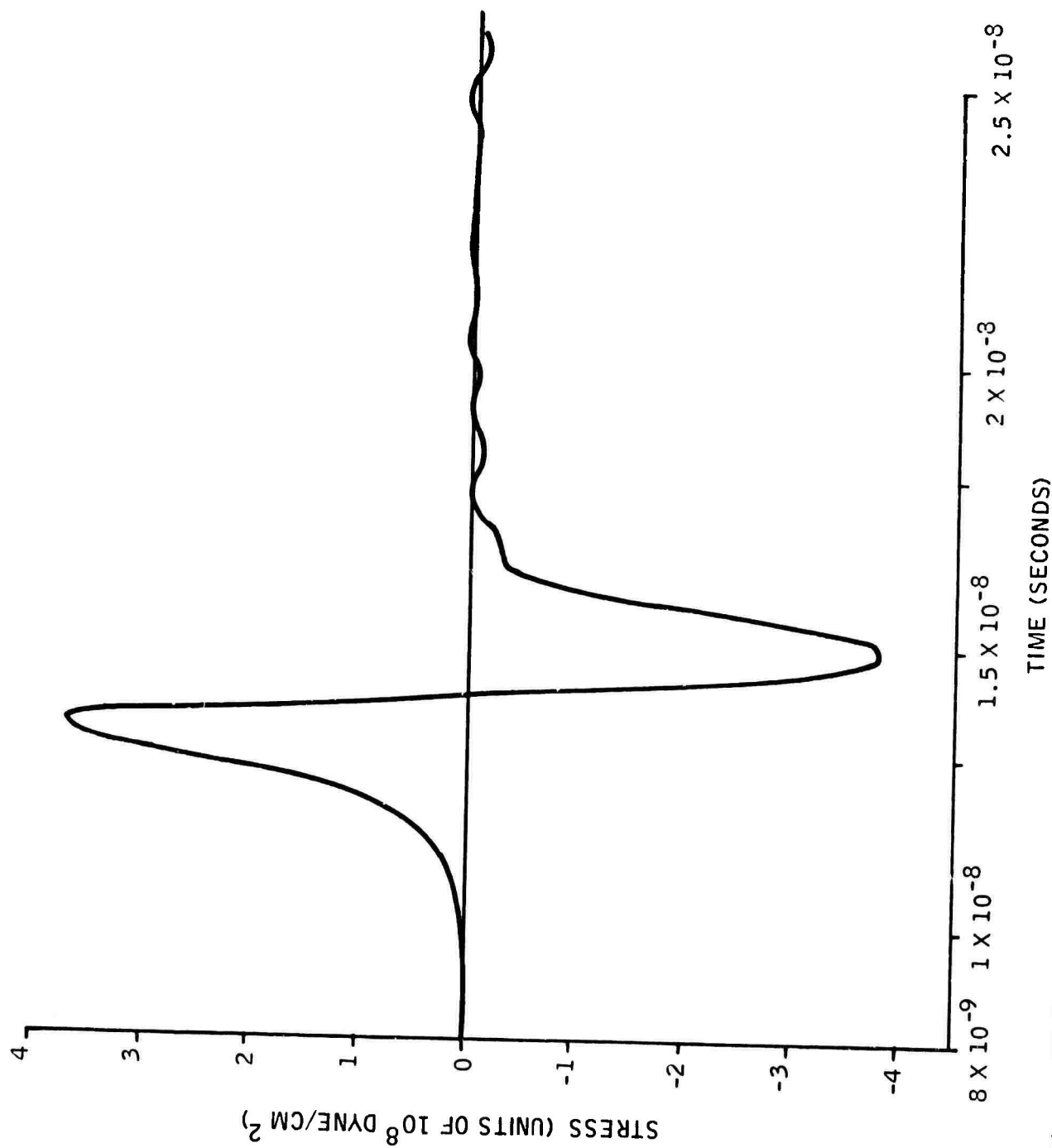


Figure III-7 - Stress as a function of time at the rear surface of a 70 micron thick sample of tungsten struck by a 30 nanosecond duration laser pulse containing  $0.3 \text{ cal/cm}^2$  as calculated by the PUFF code.

The buildup of the compressional stress wave in its early stages, at a time short compared to one nanosecond, may be seen from Figure III-6. This early buildup occurs at the depth in which the laser radiation is being absorbed. Later, as the peak pressure pulse propagates to the right, out of the depth in which the laser energy is being deposited, this buildup stops. We get the somewhat surprising result that the time history of the stress pulse is relatively independent of the power per unit area in the laser pulse, so long as the peak stress does not exceed the yield stress of the material. The general shape of the pressure pulse at the back surface will be approximately the same as that shown in Figure III-7, independent of the power per unit area delivered by the laser pulse. The amplitudes of course will change approximately linearly with the deposited energy.

As an additional check on the physical reasonableness of this interpretation, we changed the REZONE routine to allow the zones near the surface always to remain small. It was thought possible that as the peak pressure pulse propagated outside of the depth in which the laser energy was being deposited, and the zones near the surface became large, this might affect the physical nature of the problem. Therefore, we modified the REZONE subroutine so that the zones in which the laser energy were being deposited would always remain small. We found that this made no difference in the pressure pulses calculated. We interpret this as an additional check on the model that we discussed above, and as confirmation that the single sharp pressure pulse propagating into the material is a representation of physical reality rather than an artifact introduced in the computer program.

We have also considered the possibility of accounting for finer details of the thermal conduction of heat into the specimen during the laser pulse. In the work discussed above we took one single absorption coefficient characteristic of the radiation. This in effect integrated the heat deposition over the entire

laser pulse. The PUFF code has the option of allowing several spectra. If we put in a number of different spectra to represent the laser pulse, and have the different spectra active at different times, we can reproduce the effect of thermal conduction into the material during the laser pulse more exactly than by a single absorption coefficient representing the distribution of energy by thermal conduction as integrated over the entire laser pulse. For example, we break the laser pulse up into 10 intervals of 3 nanoseconds apiece, representing a total laser pulse 30 nanoseconds long. In the first three nanoseconds we choose a large absorption coefficient to represent how the energy is being deposited near the surface. For the second interval we choose a smaller absorption coefficient to represent the fact that heat has propagated farther into the material, and so on, reducing the effective absorption coefficient for each successive three nanosecond interval. In this way we can simulate conduction of heat into the material more exactly than was done in the procedure described above. The appropriate modifications in the computer program were made and the calculation carried out using effective absorption coefficients for the different spectra to represent results such as have been calculated previously<sup>(15)</sup> for the depth to which energy is conducted throughout the time of the laser pulse. These results were not significantly different from the results shown in Figure III-6. The peak pressure, the time history, and the attenuation of the sharp pressure pulse as it moves into the material were approximately the same. This means that our results are not critically dependent on the exact form of the absorption model chosen. This is reasonable and gives an added confirmation that our results represent reality instead of being a computer artifact.

### C. EXPANSION OF BLOWOFF MATERIAL

In the last semi-annual report<sup>(4)</sup> we examined the expansion of the laser produced blowoff material using a model of a one-dimensional adiabatic free expansion and found that the directed energies of the ions produced could be

higher than the thermal energies of ions in an original cloud of material at a characteristic temperature  $T_0$ . After the cloud of laser desorbed material is produced in front of the target, it will expand. If the material is hot, the original thermal energy will be transformed into energy of expansion. By fairly simple equations we determined the expansion of the gas and its cooling. The thermal energy appears at a distance from the interaction as a directed energy of expansion. The velocity of the expanding edge of the gas cloud would yield an upper limit to the energy that would be deduced from measurements on the time of flight of the particles. This energy is greater than the thermal energy originally characteristic of the particle in the gas cloud. Other workers in the field have used similar models for analysis of expansion of laser-produced blowoff material.<sup>(16)</sup>

In the last semi-annual report<sup>(4)</sup> equations were derived for the motion of the expanding edge of the gas cloud as a function of time and of original temperature of the gas. From these values the gas temperature and the particle energy corresponding to a particle traveling at the edge of the gas cloud were also derived as functions of time. This was carried out in a one-dimensional model for two postulated cases of gas density profiles. First a uniform gas density behind the edge of the cloud was assumed; second, a density gradient model was postulated in which the gas density always remained highest at the position of the surface and fell off to zero at the position of the expanding edge. The equations were evaluated numerically for the density gradient model, and data were presented on calculated particle fluxes as a function of time at a position 1 cm from the surface for various assumed initial temperatures  $T_0$ .<sup>(4)</sup> It was found that for high temperatures, of the order of 100,000°K initially, steeply rising pulses with half widths of the order of 1 or 2  $\mu$ s were predicted. These pulse shapes are very similar to those actually observed from ions in the time-of-flight spectrometer. If this model has validity, it would imply

that the blowoff material is greatly heated in a short time before it has a chance to expand. Thus this treatment has the built-in difficulty that we must provide a heating mechanism for the gas. However, the directed particle energies that are obtained are approximately seven times higher than the average value of the one-dimensional kinetic energy associated with the original assumed temperature  $T_0$ . This means, for example, that to explain the directed energies of the order of 200 eV/ion one need heat the gas only to approximately 30 eV. Moreover, this figure of 30 eV is of the same order of magnitude as the spread of energies in the spectrum deduced from the pulse shapes observed on the time-of-flight spectrometer.

In the present work we have carried out similar calculations for the uniform density model and have also expanded the whole model to take into account a more correct formulation of the boundary conditions, i. e., we have used the proper asymptotic velocity characteristic of an adiabatic free expansion.

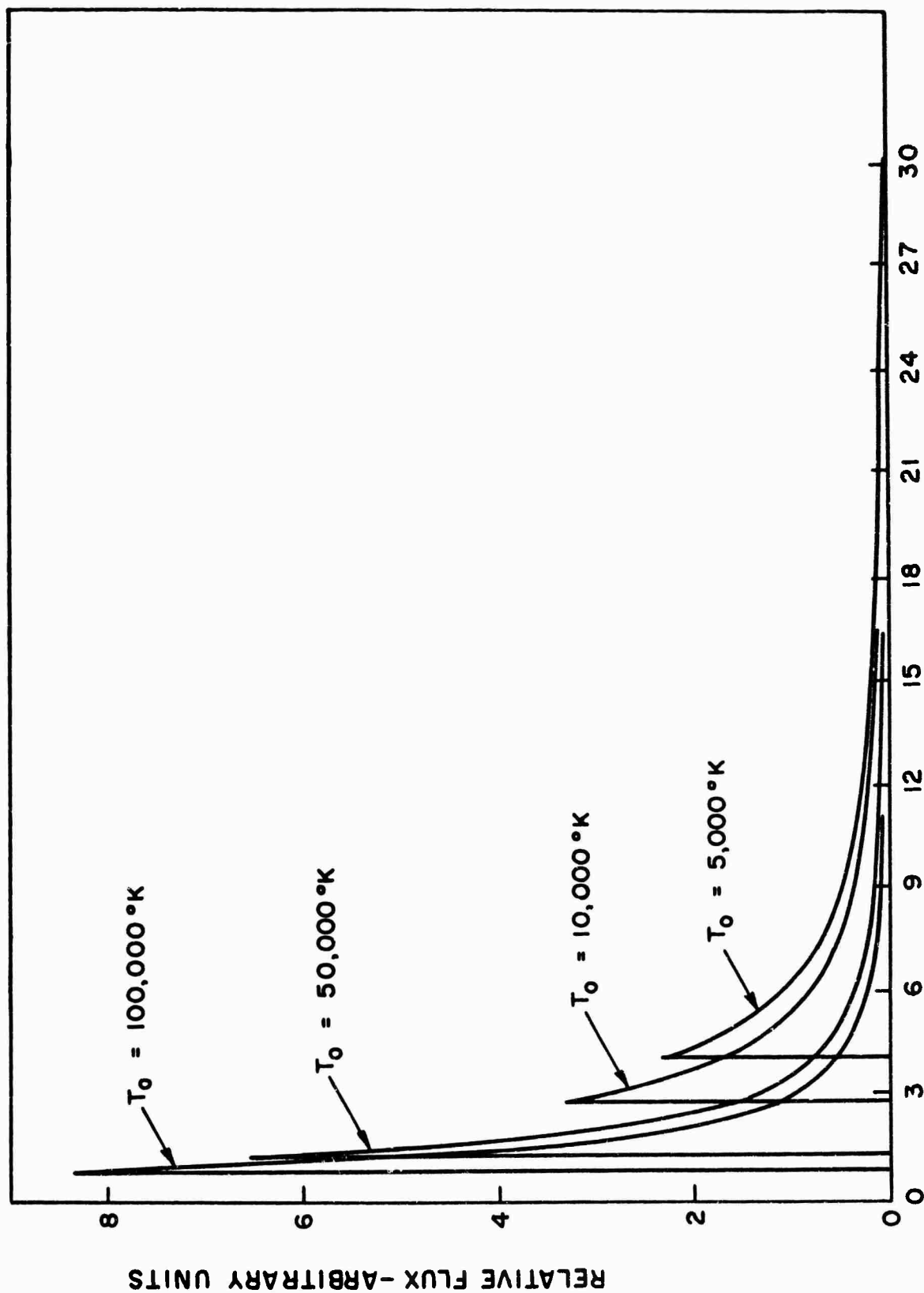
We will consider first the case in which we assumed that the blowoff material had a uniform density from the target surface out to the expanding edge of the material. The treatment for this case was developed in the last semi-annual report.<sup>(4)</sup> It relies essentially on solution of the equation:

$$\frac{d^3(X^2)}{dt^3} = 0 \quad (\text{III-6})$$

where  $X$  is the distance of the edge of the material from the surface. This equation was derived neglecting possible absorption of laser light in the blowoff material. It assumed only the existence of a cloud of gas at an original temperature  $T_0$ . The boundary conditions were taken to be that at time zero, the gas occupied a volume filling the space from the surface out to a distance equal to  $(kT_0/M)^{1/2}$  times the pulse length. Here  $M$  is the mass of the particles in the gas cloud. The velocity of the expanding edge at time zero was taken as  $(kT_0/M)^{1/2}$ , and at  $T = 0$ ,  $T_0 = \frac{MX}{3k} \frac{d^2X}{dt^2}$

In Figure III-8 we show the results for pulse shapes at a position 1 cm from the target using the uniform density model. These results were obtained by solving equation (III-6) numerically with the given boundary conditions, and give the pulse shapes due to the arrival of mass 28 ions at a position 1 cm from the target. Qualitatively, these results are very similar to those shown in Figure V-1 of the last semi-annual report where we presented analogous results obtained on the density gradient model. The pulse shapes shown in Figure III-8 indicate a vertical rise and very sharp peaks for the pulses in the uniform density model. Qualitatively, both the uniform density model and the density gradient model gives pulses that rise steeply and decay relatively slowly. In addition, both models give approximately the same relative change as the assumed value of  $T_O$  changes. As  $T_O$  increases, the pulses rise and decay faster and show decreased widths. The results for the linear density gradient model, as would be intuitively expected, give somewhat more rounded peaks which seem more physically reasonable, compared to the very sharp peaks for the pulses obtained on the uniform density model. Accordingly, our later work will consider only the density gradient model and we will not carry through the analogous derivation for the uniform density model.

The treatment described above and in the last semi-annual report for the free expansion model gives some interesting and suggestive results. However, the boundary conditions assumed for this model are subject to some question. For example, we assume that the thickness of the sheet of the blowoff material at time zero is equal to  $(kT_O / M)^{1/2}$  times the pulse length. This value may be inexact because of space charge effects as we have seen above in Section III-A. Also, the solution derived on the basis of these boundary conditions gives an asymptotic value for the velocity of expansion which is not the same as the value predicted by a more rigorous treatment of the free expansion. The details of the asymptotic solutions for the expansion of gas into a vacuum have been derived by other workers, for example E. H. Wedemeyer. <sup>(17)</sup> The results of Wedemeyer



TIME AFTER LASER PULSE (MICROSECONDS)

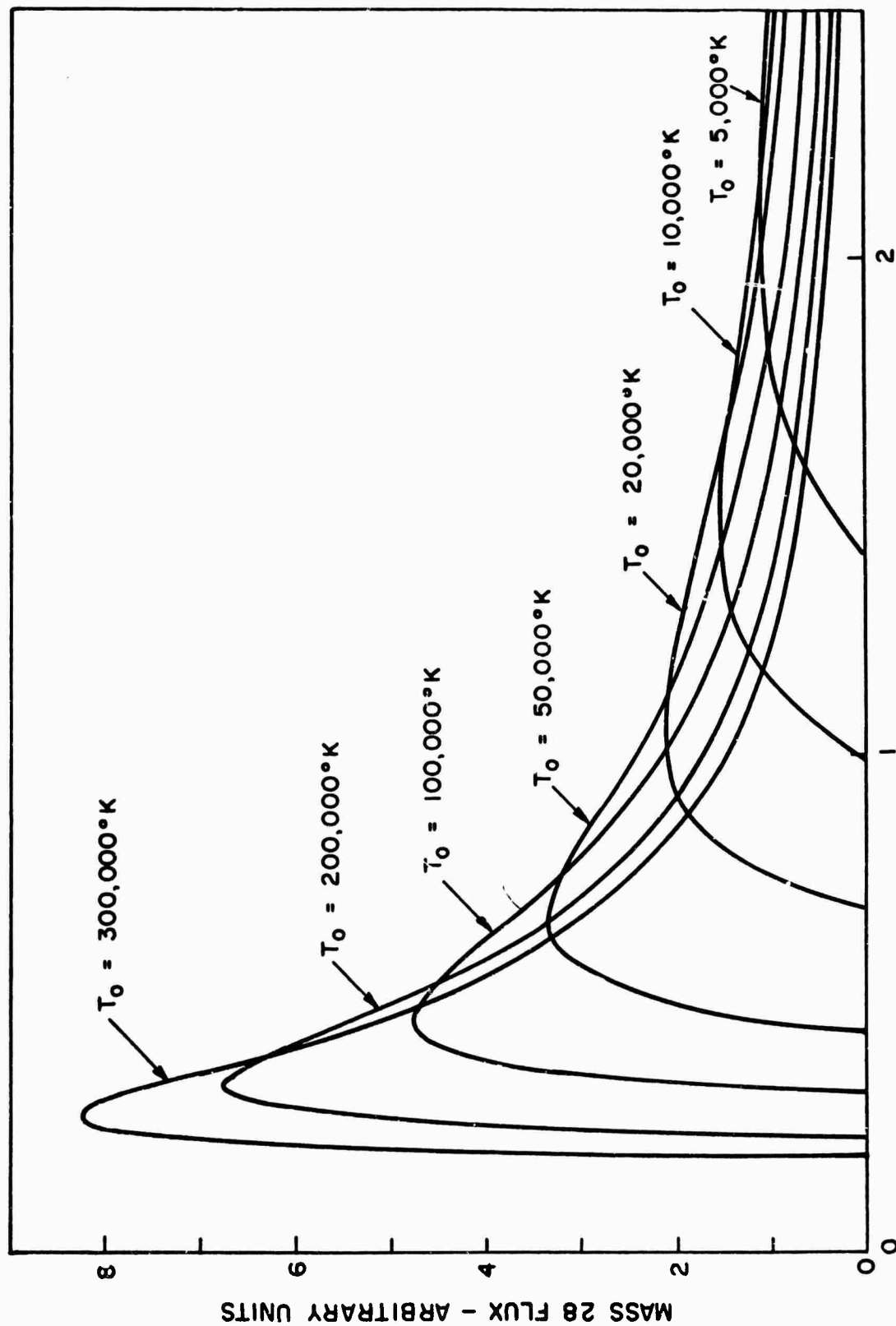
Figure III-8 Calculated mass 28 particle flux at a position 1 cm from the target based on free expansion model with uniform density assumption.

can be applied to the case of our one-dimensional geometry. It should be noted that this problem is well known. Wedemeyer's results agree with the results obtained by others. The particular thing we are most interested in is the asymptotic velocity for the adiabatic free expansion of a cloud of gas into a vacuum. If we use Wedemeyer's result we obtain an asymptotic value of the expansion velocity equal to  $2 (\gamma kT_O/M)^{1/2} / (\gamma - 1)$ . For  $\gamma = 1.4$ , a value representative of diatomic gases such as CO, one obtains  $5.91(kT_O/M)^{1/2}$ , and for  $\gamma = 1.67$ , a value representative of monatomic gases such as alkali metals, one obtains  $3.87 (kT_O/M)^{1/2}$ . In contrast, on the density gradient model we obtain  $(7kT_O/M)^{1/2}$ , and on the uniform density model we obtain  $(4kT_O/M)^{1/2}$  for the asymptotic velocity. Since the density gradient model gives more physically realistic pulse shapes, we see that our previous treatment seems to indicate asymptotic expansion velocities that are low by a factor of 2, and energies for the directed expansion that are low by a factor of 4.

The results of our density gradient model for CO and the more correct result given by Wedemeyer agree only if  $\gamma = 2.09$ . This is an unreasonably large value of  $\gamma$  for CO. Accordingly, we have modified our treatment to preserve its essential features but to give an accurate value for the expansion velocity.

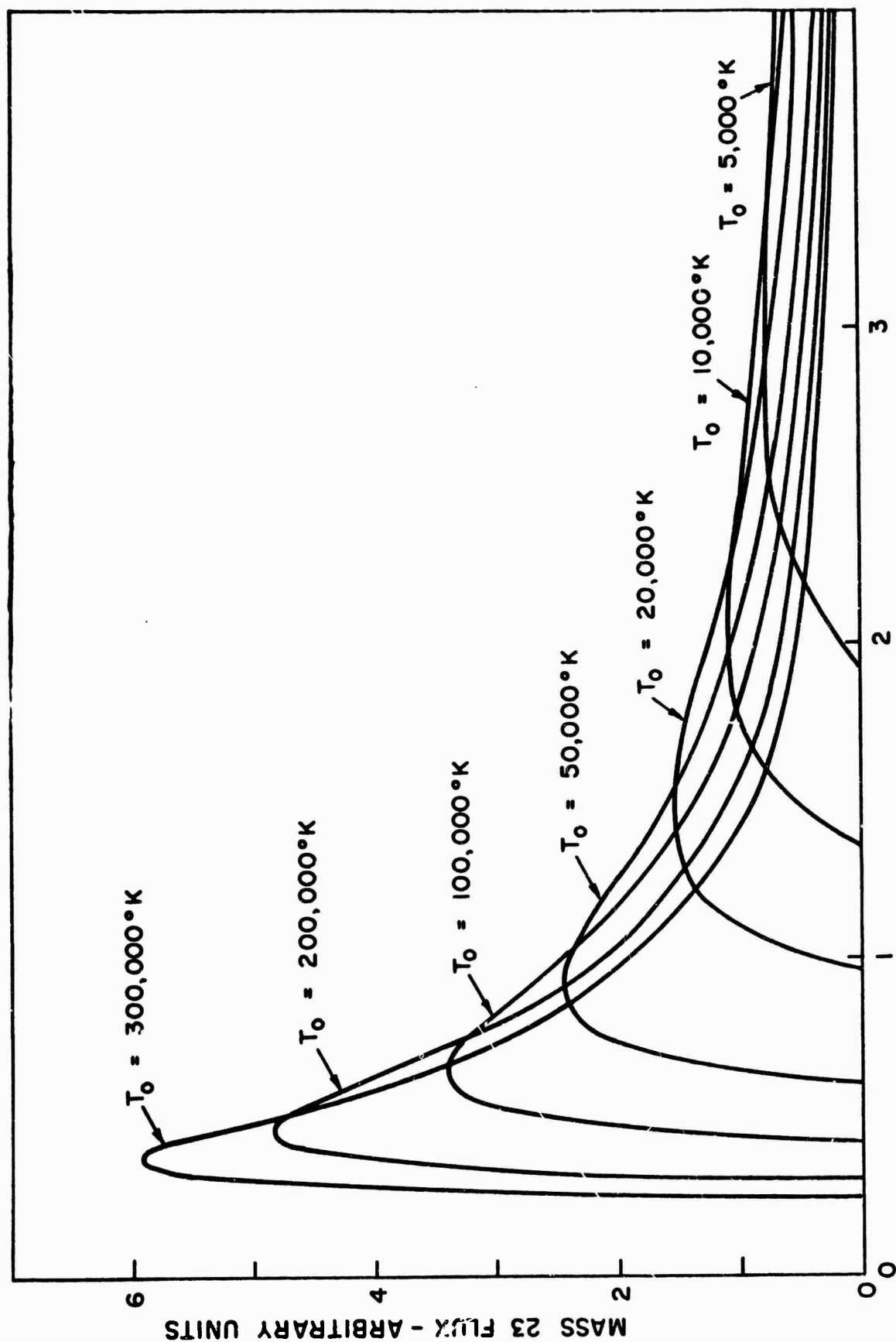
These two difficulties mentioned above can both be dealt with by using a different set of boundary conditions. Since the discussion described above in Section III-A on the thickness of the sheet of electrons in the blowoff material means that the thickness is in doubt, we discard this as a boundary condition and instead use the asymptotic value of the velocity of the expanding edge. Some results obtained by numerical integration of equation (III-6) with this boundary condition are shown in Figures III-9 and III-10. Figure III-9 shows





TIME AFTER LASER PULSE (MICROSECONDS)

Figure III-9 Calculated mass 28 particle flux 1 cm from target based on asymptotic value for free expansion with density gradient assumption.



TIME AFTER LASER PULSE (MICROSECONDS)

Figure III-10 Calculated mass 23 particle flux 1 cm from target. Based on asymptotic value for free expansion with density gradient assumption.

the pulse shape obtained at a collector 1 cm distant from the target as a function of time for the free expansion of a gas of mass 28 molecules. The original assumed temperature  $T_0$  is a parameter in these curves. These results implicitly assume the density gradient model. This figure may be compared with Figure V-1 of the last semi-annual report.<sup>(4)</sup> We see that using the asymptotic velocity of expansion as a boundary condition gives curves that generally have the same shape as those obtained with the earlier formulation. However, the asymptotic velocities are higher and the corresponding energies are also higher for a fixed initial temperature. The material begins arriving at a collector 1 cm from the target at earlier time and also the pulses are somewhat sharper with shorter width at half height. Figure III-10 shows similar results for pulse shapes for mass 23 particles. Here because of a larger value of  $\gamma$ , the corresponding energies are lower than for the case of mass 28 particles. The dominating influence here is the  $(\gamma - 1)$  term in the denominator of the asymptotic velocity.

For mass 23 particles the energy corresponding to the velocity of the expanding edge can correspond to a particle energy as high as 190 eV for an assumed  $T_0$  value of 300,000°K. If we had to explain the entire energy of 190 eV on a purely thermal basis, it would require temperatures of the order of 2 million degrees K. Thus we see that invoking a free expansion after an original heating does reduce the requirements on the heating. However, even heating to 300,000°K requires additional mechanisms which are as yet unexplained. We saw in Section III-A some considerations relating to the use of the Saha equation and conditions under which we may obtain heating by absorption of the laser light in the inverse Bremsstrahlung process. These results indicate possibly a higher heating rate than that which we calculated in earlier considerations of the same subject.<sup>(2)</sup>

The results of the present calculation on the free expansion model using the asymptotic value of the expansion velocity as a boundary condition are summed up in Table III-2 where we present the velocities and corresponding particle energies for various masses and original temperatures  $T_0$ . We see from this table that the particle energies predicted can be of the same order of magnitude as the ion energies observed in the time-of-flight spectrometer.

**TABLE III-2**  
**ASYMPTOTIC SOLUTION FOR DENSITY GRADIENT MODEL**

	$T_0$ (°K)	ASYMPTOTIC VELOCITY (CM/SEC)	ENERGY (EV)	ARRIVAL TIME AT 1 CM (μS)	TIME OF PEAK FLUX (μS)	DECAY TIME FROM PEAK TO 1/10 PEAK (μS)
MASS 2, $\gamma = 1.40$	5,000	$2.67 \times 10^6$	7.5	0.37	0.57	2.3
	10,000	$3.80 \times 10^6$	15.1	0.26	0.36	1.6
	20,000	$5.38 \times 10^6$	30.2	0.19	0.25	1.1
	50,000	$8.50 \times 10^6$	75.4	0.12	0.17	0.8
	100,000	$1.20 \times 10^7$	151	0.08	0.12	0.6
	200,000	$1.70 \times 10^7$	301	0.06	0.10	0.4
	300,000	$2.08 \times 10^7$	452	0.05	0.07	0.3
MASS 12, $\gamma = 1.67$	5,000	$7.16 \times 10^5$	3.2	1.40	2.10	8.5
	10,000	$1.01 \times 10^6$	6.4	0.99	1.49	6.3
	20,000	$1.43 \times 10^6$	12.8	0.70	1.10	4.3
	50,000	$2.26 \times 10^6$	32.0	0.44	0.64	2.8
	100,000	$3.20 \times 10^6$	64.1	0.31	0.48	1.9
	200,000	$4.53 \times 10^6$	128	0.22	0.34	1.4
	300,000	$5.54 \times 10^6$	192	0.18	0.28	1.1
MASS 23, $\gamma = 1.67$	5,000	$5.17 \times 10^5$	3.2	1.93	2.93	11.5
	10,000	$7.31 \times 10^5$	6.4	1.37	2.07	8.3
	20,000	$1.03 \times 10^6$	12.8	0.97	1.47	6.0
	50,000	$1.63 \times 10^6$	32.0	0.61	0.91	3.8
	100,000	$2.31 \times 10^6$	64.1	0.43	0.63	2.5
	200,000	$3.27 \times 10^6$	128	0.31	0.45	1.8
	300,000	$4.00 \times 10^6$	192	0.25	0.38	1.5
MASS 28, $\gamma = 1.40$	5,000	$7.19 \times 10^5$	7.5	1.39	2.09	8.7
	10,000	$1.02 \times 10^6$	15.1	0.98	1.48	6.0
	20,000	$1.44 \times 10^6$	30.2	0.70	1.10	4.0
	50,000	$2.27 \times 10^6$	75.4	0.44	0.64	2.7
	100,000	$3.21 \times 10^6$	151	0.31	0.47	1.8
	200,000	$4.55 \times 10^6$	301	0.22	0.32	1.4
	300,000	$5.56 \times 10^6$	452	0.18	0.28	1.0
MASS 39, $\gamma = 1.67$	5,000	$3.97 \times 10^5$	3.2	2.52	3.82	15.5
	10,000	$5.61 \times 10^5$	6.4	1.78	2.68	10.9
	20,000	$7.94 \times 10^5$	12.8	1.26	1.86	7.9
	50,000	$1.26 \times 10^6$	32.0	0.80	1.20	4.8
	100,000	$1.78 \times 10^6$	64.1	0.56	0.86	3.4
	200,000	$2.51 \times 10^6$	128	0.40	0.60	2.4
	300,000	$3.08 \times 10^6$	192	0.33	0.49	2.0

In summary, the picture that can be deduced from this analysis is consistent with the high energy ion pulses being produced by expansion of a heated gas cloud provided that the desorbed gas can be heated rapidly during the laser pulse. This leads to energies of expansion with superimposed random components of the same order of magnitude as we actually observe in the time-of-flight spectrometer, and also to pulse shapes similar to those obtained experimentally. We shall consider some of the speculations concerning a synthesis of the processes occurring in the blowoff material as derived from both the time-of-flight spectrometer and the quadrupole spectrometer measurements in Section III-E, and will consider the mechanism of heating that could occur.

Further work on the expansion of the laser produced blowoff material will include the following steps:

1. Inclusion of the effect of an accelerating potential. In our actual measurements on the time-of-flight spectrometer, ions are accelerated across the gap by an applied field of the order of kilovolts. This applied field also repels the electrons into the target and affects the space charge sheath near the target. It will be necessary to include the effect of the space charge and also the motion of the entire cloud of ions away from the target surface. In this formulation the density gradient model as we have set it up previously will no longer be applicable.
2. Inclusion of drift time down the drift tube in the time-of-flight spectrometer. When this drift time is included, we will obtain pulse shapes that can be compared directly to experimental pulse shapes.

3. Inclusion of possible absorption in the plasma. Equation (III-6) can be modified to include a term for possible absorption in the plasma. The right hand side will be non-zero. The conjectures described previously about the heating rate may be higher than we considered it to be in earlier calculations and will give us insight into how this whole routine can be modified to include the effect of heating during the early stages of the expansion. This whole formulation would then have to be solved numerically in order to give a complete picture of how the blowoff material heated and expanded.
4. In the computer runs in which the results, such as are shown in Figures III-9 and III-10, were calculated we found that the velocity of the expanding edge very rapidly approached the asymptotic velocity. In fact, within only a few nanoseconds after the material began expanding it had reached the asymptotic velocity and most of the distance from the target to the distance 1 cm away was covered at this asymptotic velocity. This means that the picture of a 30 nanosecond long pulse in which the blowoff material is produced, and raised to a temperature  $T_0$ , and then expands, cannot be realistic since the time of transition from the original state to the asymptotic state is shorter than the time we consider the material as remaining in its initial state. Our future work will take this fact into account and consider simultaneous heating and expansion.

#### D. ELECTRON EMISSION

Calculations have been carried out on the electron emission from a laser heated surface. These calculations are essentially a return to work done some time ago.<sup>(18)</sup> We had found a discrepancy between calculated temperatures based on thermodynamic considerations and observed temperatures as deduced from the electron emission in the laser-heated

spot using Richardson's equation. In particular, as seen from Figures 3 and 4 of reference <sup>(18)</sup>, the experimentally deduced temperatures consistently ran several hundred degrees higher than the theoretically calculated temperatures. At the time we hypothesized that the reason for this discrepancy was that the power density in a laser beam was not uniform. This non-uniformity gave local hot spots in the laser beam and contributed largely to the emission because of the non-linear dependence of the electron emission on temperature. These local hot spots dominate the emission to the extent that it makes the average temperature look higher than it actually is. Most of the electron emission arises from the area near the center of the laser beam where the temperature is highest. Even though this is a relatively small fraction of the area, the dependence of the electron emission is so strongly a function of temperature that when the total electron emission is divided by the total area, one obtains a value for the average emission that corresponds to a temperature higher than the average temperature of the surface.

In the present work we used the spatial distribution of power in the laser pulse as described in a previous report, <sup>(1)</sup> and set up a calculation for a laser power distribution with this shape. The treatment here is similar to the calculation of the desorption of carbon monoxide from a tungsten surface as described in a previous report. <sup>(2)</sup> In that work we started with a known rate of desorption of carbon monoxide as a function of temperature. The temperature was then calculated as a function of position and time for a laser pulse with specified spatial and temporal shapes, and numerically integrated to obtain the total desorption of carbon monoxide. In the calculation it was assumed that there was essentially no transverse flow of heat in the laser-heated spot. In other words, the transverse dimensions of the spot were much greater than the depth of penetration of the heat during the time of the laser pulse. This condition is reasonably well approximated for our work. It means that the rise in temperature at a position in the laser heated spot is directly proportional to the input power density at that position.

For the electron emission as a function of temperature at a particular position in the laser spot we used Richardson's equation. For the laser power density as a function of position we used the distribution described previously.<sup>(1)</sup> As a function of the radius  $r$  from the center of the spot and the polar angle  $\theta$ ,

$$P(r, \theta) = P_0 \left[ 1 - \frac{r}{\alpha (n - \sin 2\theta)} \right]$$

$P_0$  is the power per unit area at the center of the illuminated area.

Here the approximate values of  $n$  and  $\alpha$  are  $n = 4$ , and  $\alpha = 0.075$  cm. The variables in the temperature  $T(r, \theta, t)$  may be separated according to the formulation described above in which the temperature rise at a particular position is linearly proportional to the power density at that particular position under the assumption that there is no transverse flow of heat. In other words,  $T(r, \theta, t)$  equals  $P(r, \theta)$  times the temperature as a function of time for a unit power uniform spatial distribution laser pulse with the desired temporal shape. With this formulation the electron current as a function of time is:

$$J(t) = AP_0^2 T_1^2(t) \int_0^{2\pi} d\theta \int_0^{(n + \sin 2\theta) \alpha} \left[ 1 - \frac{r}{\alpha (n + \sin 2\theta)} \right]^2 \exp \left\{ \frac{-\phi}{k (T_0 + P_0 T_1(t))} \left[ 1 - \frac{r}{\alpha (n + \sin 2\theta)} \right]^{-1} \right\} r dr$$



In this equation  $A$  is the constant in Richardson's equation,  $T_1(t)$  is the temperature for a spatially uniform laser pulse of unit power with the desired temporal shape,  $P_O$  is the peak laser power per unit area at the center of the laser spot at the time at which the laser power is highest,  $\phi$  is the work function of the surface,  $k$  is Boltzman's constant,  $T_O$  is the initial temperature, and the other variables are defined above. This equation, by suitable manipulation, can be reduced to the following form:

$$J(t) = AP_O^2 T_1^2(t) \alpha^2 \pi (2n^2 + 1) \\ \times \left[ -\frac{e^{-a(t)}}{4} + \left(1 + \frac{a(t)}{4}\right) \left(\frac{e^{-a(t)}}{3} - \frac{a(t)e^{-a(t)}}{6} + \frac{a^2(t)e^{-a(t)}}{6} + \frac{a^3(t)}{6} E_1(a(t))\right) \right]$$

Here  $a(t) = \phi/k (T_O + P_O T_1(t))$ , and  $E_1(a(t))$  is the exponential integral.

We have used values for  $T_1(t)$  taken from earlier calculations,<sup>(15)</sup> for a laser pulse shape actually representative of that which was used in the electron emission experimental work.<sup>(18)</sup> The above equation was then evaluated on a computer using a numerical routine for evaluation of  $E_1(a(t))$  with the values of  $T_1(t)$  stored in memory. Some results are shown in Figure III-11, where we see the electron emission from tungsten as calculated on this basis of nonuniform spatial power distribution. The parameter is the laser power at the peak value in time divided by the area of the illuminated spot.

One may take results such as shown in Figure III-11 and use the known values for thermionic emission as a function of temperature and deduce an apparent temperature corresponding to the average value of electron emission over the whole spot. This is the quantity that we compare to an experimentally deduced temperature from the laser emission. The results are shown in Figure III-12 for thoriated tungsten. This is essentially a modification of Figure 3 of the reference (18). The present version of this figure gives a postulated laser power as a function of time. This is the total laser power divided by the total

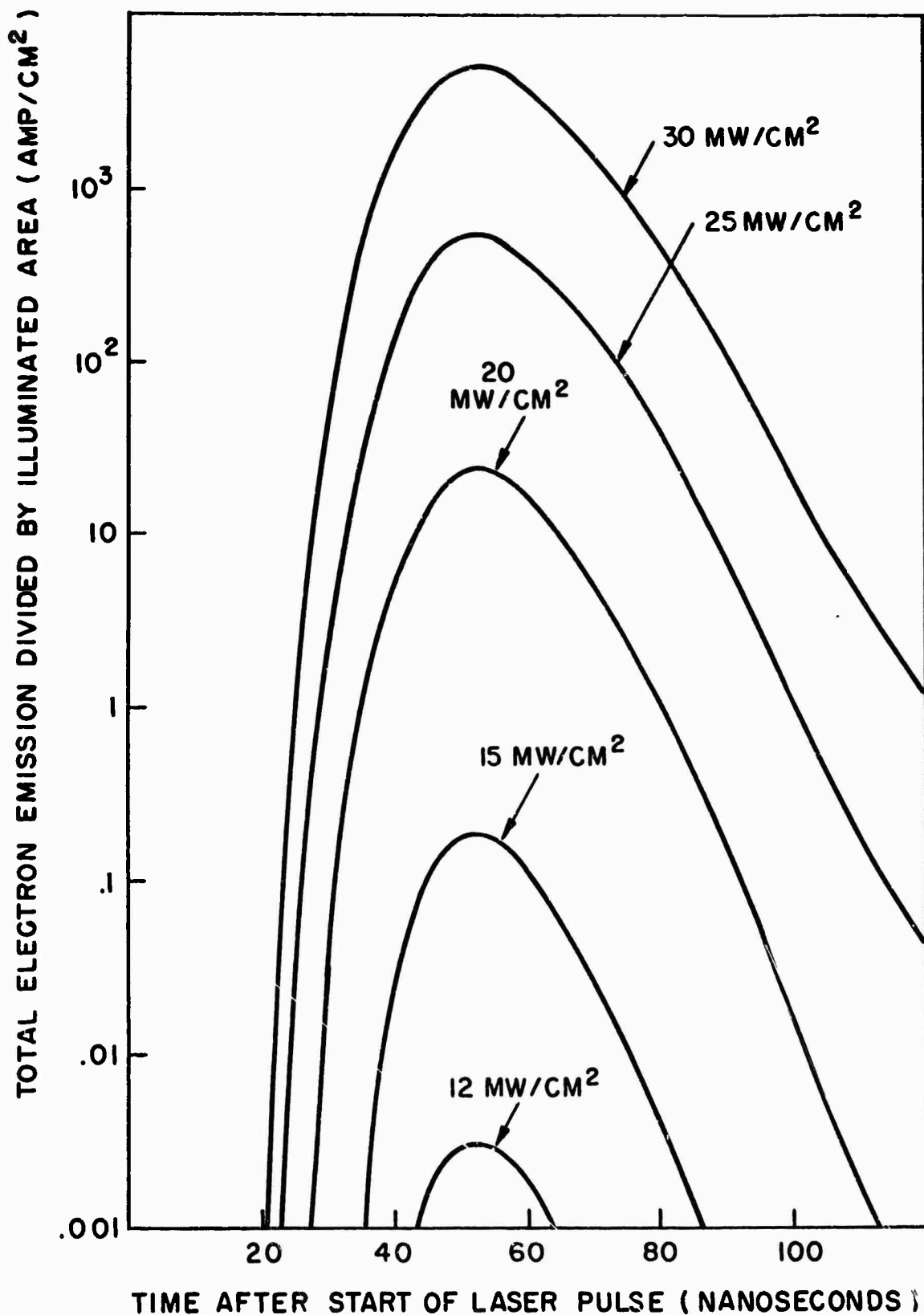


Figure III-11 Electron emission from tungsten calculated for non-uniform power distribution for a laser pulse 100 nanoseconds long, with peak power 30 nanoseconds after its start. Parameter is the laser power (at 30 nanoseconds after the start of the pulse) divided by the illuminated area.

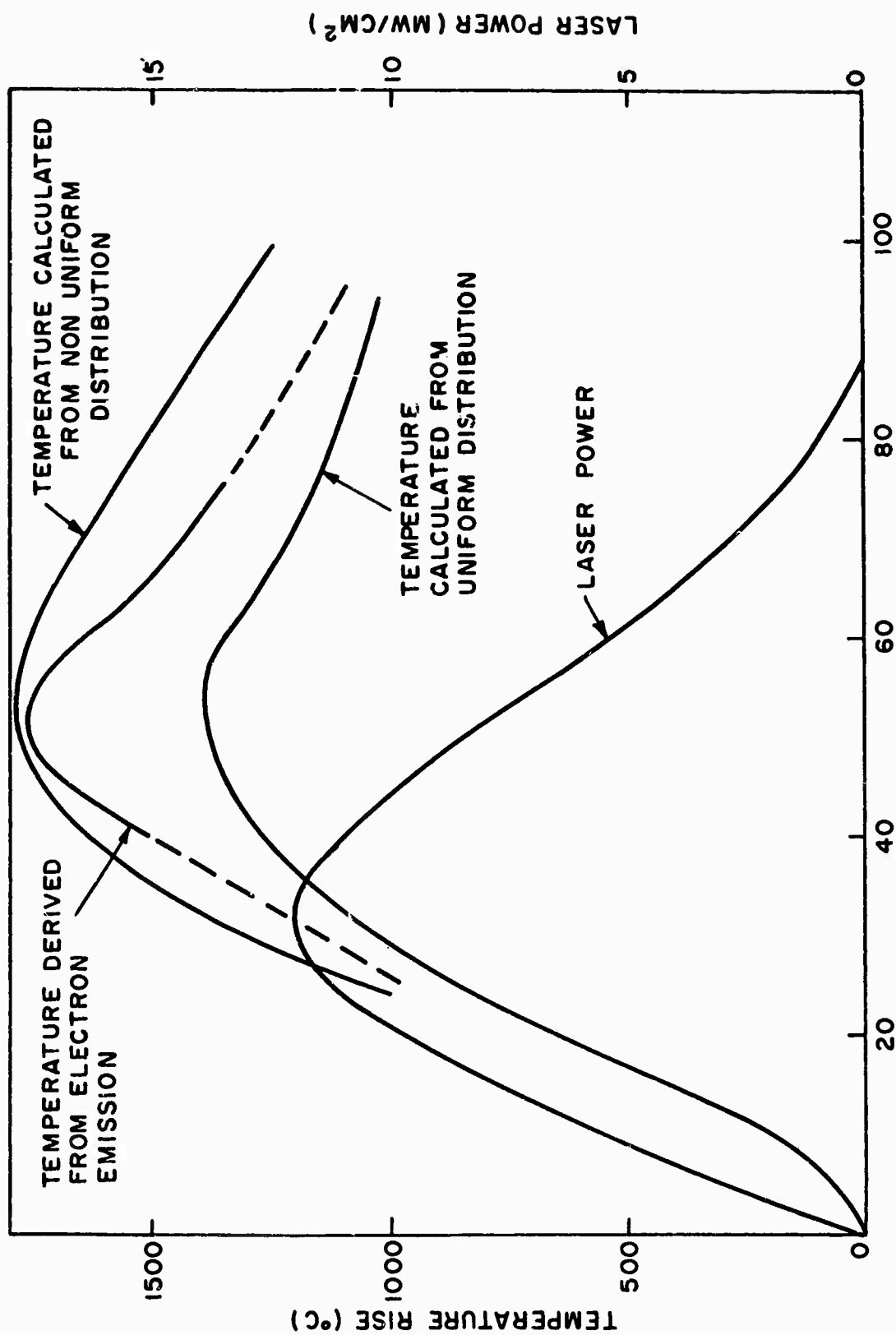


Figure III-12 Apparent temperature of thoriated tungsten surface as derived from calculation and from experiments on electron emission for a laser pulse of the given shape. Right scale is total laser power divided by illuminated area.

area of the spot. Figure III-12 shows the experimental temperature as derived from the measured values of the electron emission, and also two theoretical values, first the theoretical value obtained from assuming that the laser power is uniform over the spot, and second the theoretical value as modified for the nonuniform temperature distribution as described above. We see that in this particular power range (peak power around 12 megawatts/cm<sup>2</sup> average value) using the spatial distribution actually representative of our laser pulse gives a temperature value several hundred degrees higher than the temperature calculated assuming a uniform spatial distribution. This calculated temperature is in quite good agreement with the experimentally determined temperature as a function of time.

For laser powers of approximately 10 to 15 MW/cm<sup>2</sup> good agreement is obtained between the presently modified theory and the experiment. However, at higher powers the theoretical values are rising faster than the experimental values. This occurs because the center of the spot becomes very hot, and because of the non-linear dependence of electron emission on temperature. Thus the values calculated on the present theoretical formulation become much higher than the experimentally determined values at laser powers of the order of 20 to 25 MW/cm<sup>2</sup>. This can be explained by saturation of the experimentally obtained current as the current becomes very high. Space charge effects limit the experimental current as the temperature at the center of the spot rises. In the earlier work<sup>(18)</sup> we had a collecting voltage high enough to overcome space charge effects at laser powers around 15 MW/cm<sup>2</sup>. However, at the higher laser powers at the center of the spot we can have enough space charge effect so that we no longer can pull all the electrons over to the collector.

In summary, using experimentally determined spatial distributions for the laser power density gives good agreement between theoretical and experimentally determined values of the temperature at the low end of the range of laser powers used in the electron emission experiments. However, at higher powers of the order of  $20$  to  $25 \text{ MW / cm}^2$ , at the upper end of the range of laser power densities used in the experimental electron emission, there still remain discrepancies between theory and experiment.

#### E. PARTICLE EMISSION IN LASER-SURFACE INTERACTIONS

A coherent picture of the entire system of particles produced in a laser-surface interaction as obtained from the combined results of measurements on the time-of-flight spectrometer and the quadrupole spectrometer may be synthesized to explain the range of phenomena observed.

The ideas presented in this subsection are preliminary and speculative. We do not have proof of all the hypotheses given here. They do appear to be physically appealing and are consistent with our experimental results, but further work will be required to provide more definite proof.

As the surface is heated, we get emission of neutral gases such as CO, of alkali metals emitted as ions, for example, sodium and potassium ions, and also, at our power densities, a relatively small amount of the base material such as tungsten. This is accompanied by a fairly large amount of thermionic electron emission. The electrons set up a space charge sheath near the surface in a fairly short time. The equilibrium time during which this sheath is set up can be very short because of the high mobility of the electrons, and we can reach a steady state even during the time of the laser pulse. This local region of high charge density can lead to high rates of heating.

In particular, we look on the sodium ions as being rapidly heated by absorption of the laser light in the inverse Bremstrahlung process in this localized region of high charge density. Most of the material does not heat to high temperatures. This is evidenced by the fact that the CO is emitted mainly as undissociated molecules.

We consider the main mechanism of energy transfer to be through electron collisions. We consider the electron collisions to be rapid enough that thermal equilibrium can be established on a local basis between the electrons and the ions, but the interaction of electrons and neutral particles to be slow enough that essentially little heating of the neutral molecules can occur. Thereafter we can have elastic collisions between energetic sodium ions and the thermal CO molecules. This will lead to some dissociation of the CO but there will also be elastic collisions in which high energy CO molecules will be produced.

Relative numbers of the various components will have to agree with this picture. In particular, we should see much more thermal CO than any other component. Also, collisions with the hot sodium ions should produce dissociation of some of the CO. Thus, we should see some low energy carbon and oxygen produced in the dissociation interactions. We should also see a smaller amount of high energy CO molecules. Experimentally the numbers of high energy CO molecules that we observe is somewhat in doubt because of uncertainty about the secondary emission coefficient of the photocathode for energetic molecules. However, the results are not inconsistent with their being many fewer high energy CO molecules than thermal CO molecules. This is the case if the secondary emission coefficient approaches unity. This picture is also supported by the observation that the high energy CO typically has about half as much energy as the high energy ions, as might be expected if they were produced in elastic collisions with energetic alkali ions.

This picture synthesizes the main features of the observations made on two different types of spectrometers. It provides a plausible heating mechanism for the energetic ions that are in fact observed, but allows most the material to remain cool. The mechanism for the high energy neutral molecules observed is assumed to be elastic scattering from high energy alkali ions. The directed energy of the center of mass of the entire system is assumed to come from an adiabatic free expansion.

This picture must be regarded as preliminary, but it does combine enough features to explain the results obtained on both types of spectrometers, and has physically appealing reasons to back it. The great question is whether there is enough heating possible to heat the ions to the required high temperatures. If so, we can, as we saw in Section III-C, explain the pulse shapes, the directed energies, and the superimposed random components of energy for the alkali ion pulses observed in the time-of-flight spectrometer. The reasoning given in Section III-A will be developed further to obtain quantitative estimates of the heating for our experimental conditions in order to answer this question.

## SECTION IV

### SUMMARY

The work described in this report deals with a number of related topics relevant to the laser-surface interaction. The experimental and theoretical work complement each other and will lead to an understanding of the nature of the processes occurring when a high power laser beam strikes a metallic surface. Some of the topics described here are extensions of measurements or calculations which have been carried out previously as part of this continuing effort, for example, measurements on the ion and neutral molecule emission from sodium targets, and calculations on the particle pulse shapes resulting from a free expansion of the heated blowoff material. Other topics are introduced in this report for the first time; for example, measurements of the angular distribution of the ionic emission, and calculation of thermomechanical stress profiles in the target.

At this point we stand at a transition phase in this work, with earlier types of measurements essentially being completed, and new types of measurements yielding preliminary results. The earlier work, on ion and neutral gas emission from various surfaces at relatively low laser powers (of the order of  $50 \text{ MW/cm}^2$ ), which relied mainly on the quadrupole and time-of-flight mass spectrometers, is being replaced by other types of measurements on new equipment designed to elucidate specific features of the laser-surface interaction, for example, the angular distribution of ion emission. The capability of extending the measurements to a higher range of laser powers has also been developed. We have also reached the stage where the various results, both theoretical and experimental, can be integrated to provide a complete picture of the phenomena occurring in the laser-produced blowoff material, whereas the earlier work tended to consider one specific phenomenon at a time.



The specific results described in this report include the following as the most significant:

1. Preliminary indications of an anisotropy in the ion emission, with most ions emitted in the direction normal to the surface.
2. Measurements on sodium targets, indicating large sodium ion and hydrocarbon fragment emission.
3. Refinement of calculations on the free expansion of the blow-off material, indicating that the results for an initial temperature around  $10^5$  K are similar to the pulse shapes, including the directed velocity component, of the observed ion emission.
4. Investigations of the space charge effects and ionization levels in the blowoff material, with implications relative to the possible heating of this material by the laser light.
5. Preliminary formulation of an integrated picture to describe experimental results from both the time-of-flight and quadrupole spectrometers, in which heating occurs in a plasma of alkali ions, while the neutral gas remains cool.
6. Calculation of thermomechanical stress profiles in the target material due to absorption of the laser light, in which, for our experimental conditions, the main feature is a sharp pressure spike of the order of  $6 \times 10^8$  dyne/cm<sup>2</sup> propagating into the target.

For the future, plans call for completing and extending the work described above. Specifically we shall complete the investigation of the angular distribution of the ion emission and carry out a critical experiment to

determine the role of the absorption of the laser light in heating the blowoff material. We shall extend the measurements into a higher range of laser powers than has been used previously. The plasma heating mechanism will be investigated in the light of the considerations of ionization levels in the blowoff material as described above. These results will be integrated with the work on expansion of the blowoff material in order to analyze the formulation for the picture of the particle emission as described in Section III-E. The calculations on the shock waves generated in the targets will be extended to include other target materials.

## REFERENCES

1. "Mechanisms of Laser-Surface Interactions", by J. F. Ready, E. Bernal G., L. P. Levine, Final Report to Ballistic Research Laboratories on Contract DA-11-022-AMC-1749(A), March 1965. (AD-467, 867)
2. IBID, Semi-Annual Report on Contract DA-11-022-1749 (A) Mod 2, November 1965. (AD-477, 231)
3. IBID, Final Report on Contract DA-11-022-AMC-1749 (A) Mod 2, May 1966. (AD-636, 680)
4. IBID, by J. F. Ready and E. Bernal G., Semi-Annual Report on Contract. DA-18-001-AMC-1040 { X } December, 1966. (AD-645, 473).
5. G. A. Hardway, MicroWaves, April, 1966, p. 46.
6. N. I. Sax, "Dangerous Properties of Industrial Materials", Reinhold Publishing Corp., New York, N. Y., 1962.
7. J. D. Ryder, "Electronic Fundamentals and Applications", Prentice-Hall (1950).
8. L. Spitzer, "Physics of Fully Ionized Gases", Interscience (1956).
9. H. R. Griem, "Plasma Spectroscopy", McGraw-Hill (1964).

10. C. E. Moore, Atomic Energy Levels, Vol. I, National Bureau of Standards Circular 467, June 15, 1949.
11. K. D. Pyatt and J. R. Triplett in LASCON II, Proceedings of the 2nd Classified Conference on Laser Technology, Chicago, 1965. (Available as AD-361, 398 L.)
12. D. W. Gregg and S. J. Thomas, J. Appl. Phys. 37, 2787 (1966).
13. R. N. Brodie and J. E. Hormuth, AFWL-TR-66-48, May 1966. (Available as AD-482, 409.)
14. See, for example, J. M. Walsh, et. al., Phys. Rev. 108, 196 (1957); R. G. McQueen and S. P. Marsh, J. Appl. Phys. 31, 1253 (1960); M. H. Rice, R. G. McQueen, and J. M. Walsh, Solid State Physics 6, 1 (1958).
15. J. F. Ready, J. Appl. Phys. 36, 462 (1965).
16. A. F. Haught and D. H. Polk, Physics of Fluids 9, 2047 (1966).
17. E. H. Wedemeyer, Ballistics Research Laboratories Report No. 1278, April, 1965.
18. J. F. Ready, Phys. Rev. 137, A620 (1965).

Unclassified  
Security Classification

DOCUMENT CONTROL DATA - R & D

(Security classification of title, body of abstract and indexing annotation must be entered when the overall report is classified)

1. ORIGINATING ACTIVITY (Corporate author) Honeywell Inc. Corporate Research Center Hopkins, Minnesota		2a. REPORT SECURITY CLASSIFICATION Unclassified	
2b. GROUP			
3. REPORT TITLE  MECHANISMS OF LASER-SURFACE INTERACTIONS			
4. DESCRIPTIVE NOTES (Type of report and inclusive dates) Final Report			
5. AUTHOR(S) (First name, middle initial, last name) J. F. Ready, E. Bernal G., and L. T. Shepherd			
6. REPORT DATE May 1967	7a. TOTAL NO. OF PAGES 90	7b. NO. OF REFS 18	
8a. CONTRACT OR GRANT NO. DA-18-001-AMC-1040(X)	8b. ORIGINATOR'S REPORT NUMBER(S)		
8c. PROJECT NO.	8d. OTHER REPORT NO(S) (Any other numbers that may be assigned this report)		
10. DISTRIBUTION STATEMENT  Distribution of this document is unlimited.			
11. SUPPLEMENTARY NOTES		12. SPONSORING MILITARY ACTIVITY  U.S. Army Ballistic Research Laboratories Aberdeen Proving Ground, Md. 21005	
13. ABSTRACT  This report describes experimental and theoretical investigations of the particle emission produced in the laser-surface interaction. Preliminary measurements on the angular distribution of ions emitted from a tungsten target at power levels around 14 MW/cm <sup>2</sup> indicate anisotropy of the emission, with a strong enhancement in directions near the normal to the target. Ion and neutral molecule emission from laser-irradiated sodium targets are described. Calculations on the free expansion of the laser-produced blow off material, which include the asymptotic velocity of the expansion, yield pulse shapes similar to those observed experimentally if a high initial temperature is assumed. The magnitudes and time histories of shock waves produced in the target by absorption of the laser radiation have been calculated.			

DD FORM 1473  
NOV 55

REPLACES DD FORM 1473, 1 JAN 54, WHICH IS  
OBSOLETE FOR ARMY USE.

Unclassified  
Security Classification

Unclassified  
Security Classification

14.	KEY WORDS	LINK A		LINK B		LINK C	
		ROLE	WT	ROLE	WT	ROLE	WT
	Laser Effects Plasma Ion Angular Distribution						

Unclassified  
Security Classification